W. Fundamenski, O.E. Garcia, V. Naulin, R.A. Pitts, A.H. Nielsen,
J Juul Rasmussen, J. Horacek, J.P. Graves and JET EFDA contributors

Neoclassical Dissipation and Parallel Losses in Interchange Driven Scrape-Off Layer Turbulence

Neoclassical Dissipation and Parallel Losses in Interchange Driven Scrape-Off Layer Turbulence

W. Fundamenski[1], O.E. Garcia[2], V. Naulin[2], R.A. Pitts[3], A.H. Nielsen[2],
J Juul Rasmussen[2], J. Horacek[3], J.P. Graves[3] and JET EFDA contributors*

[1]*EURATOM/UKAEA Fusion Association, Culham Science Centre, Abingdon, OX14 3DB, UK*
[2]*Association Euratom–Risø National Laboratory, OPL-128 Risø, DK-4000 Roskilde, Denmark*
[3]*Centre de Recherches en Physique des Plasmas, Association Euratom–Confédération Suisse,
EPFL, CH-1015 Lausanne, Switzerland*
** See annex of J. Pamela et al, "Overview of JET Results",
(Proc. 20th IAEA Fusion Energy Conference, Vilamoura, Portugal (2004).*

ABSTRACT.

First principles expressions are given for the parameters governing collisional diffusion and parallel losses of mass, momentum and energy in tokamak Scrape-Off Layer (SOL) plasmas. These transport coefficients are based on neoclassical perpendicular transport (Pfirsch-Schlüter diffusion) and classical parallel transport (sub-sonic advection and Spitzer- Härm diffusion). When numerical values derived from these expressions are used to compute damping coefficients for the electrostatic edge-SOL (ESEL) turbulence code, simulations correctly reproduce the radial profiles of particle density, n, and electron temperature, T_e, as well as statistical distributions and temporal correlations of particle density and flux density measured in Ohmic and L-mode plasmas on the TCV tokamak. Similarly, preliminary calculations agree reasonably well with radial profiles of n and T_e measured in Ohmic and L-mode plasmas on JET, although the far-SOL particle density e-folding length is broader by a factor of 3 than the measured value. The overall agreement between simulation and experiment suggests that turbulent SOL transport is driven by interchange motions, caused by unfavourable curvature and strong pressure gradients in the edge region, with the level of turbulence being influenced by neoclassical diffusion and parallel losses in the SOL region.Moreover, the curvature drive offers a viable mechanism for the origin of the $\mathbf{B} \times \nabla B$-independent part of the parallel SOL flow measured on many tokamaks, including JET and TCV tokamaks, with ESEL simulation predicting a parallel Mach number of ≈ 0.2 in JET Ohmic and L-mode plasmas, in fair agreement with Mach probe measurements.

1. Introduction

The exhaust of particles and power without undue damage to the vessel walls is one of the critical issues for burning plasma tokamaks such as the planned ITER experiment. This exhaust is determined by competition between *parallel* and *perpendicular* transport in the region of open field lines beyond the magnetic separatrix, known as the scrape-off layer (SOL). Whereas parallel transport is largely classical and well understood, radial transport in the SOL is generally turbulent, with relative fluctuations often exceeding unity [1, 2]. Moreover, isolated structures, variously known as *blobs* or *filaments*, which carry particles, momentum and energy into the far-SOL are universally observed as intermittent bursts in single-point recordings of plasma parameters and in two-dimensional imaging of the edge and SOL plasmas [3–11].

Recently, dedicated experiments in Ohmic and L-mode plasmas on the TCV tokamak [8,9] have shown that SOL intermittency, which can be quantified using statistical techniques, increases with radial distance away from the separatrix, so that probability distribution functions (PDFs) of the particle density become increasingly skewed. In a separate study, the TCV-measured SOL turbulence statistics have been very well reproduced by curvature driven interchange turbulence simulations based on three fields: particle density, electric potential and electron temperature, (n, ϕ, T_e), in the two-dimensional plane perpendicular to the magnetic field – the so-called *drift plane* [10]. In that work, the coefficients representing collisional diffusion and parallel losses were treated as free parameters and were adjusted to obtain a satisfactory match with the TCV data. Specifically, no attempt was made to justify the values of these coefficients, nor to discuss their physical basis.

In this article, we derive first principles expressions for these coefficients and find them to agree closely with the values used to match the TCV data in [10], with the exception of a much lower predicted value of the particle diffusivity. Subsequent simulations, incorporating the newly derived expressions, further improve the overall agreement between model and experiment [11]. It is worth emphasizing that the obtained expressions are applicable to both limiter and divertor configurations and are relevant to all edge–SOL turbulence simulations, which should aim to describe neoclassical dissipation and parallel losses in a realistic manner. Finally, first simulations of JET Ohmic and L-mode plasmas are presented, showing fair agreement with radial SOL profiles of particle density, temperature and the $\mathbf{B} \times \nabla B$-independent (ballooning) component of the parallel Mach number.

2. Electrostatic interchange turbulence model

2.1. Governing equations of the ESEL code

We begin the analysis by introducing the reduced fluid equations for low-frequency (drift ordered) dynamics of n, ϕ and T_e as derived and discussed in [12–14],

$$\frac{\mathrm{d}n'}{\mathrm{d}t'} + n'\mathscr{C}'(\phi') - \mathscr{C}'(n'T'_e) = \Lambda'_n, \tag{1a}$$

$$\frac{\mathrm{d}T_\mathrm{e}'}{\mathrm{d}t'} + \frac{2}{3}T_\mathrm{e}'\mathscr{C}'(\phi') - \frac{7}{3}T_\mathrm{e}'\mathscr{C}'(T_\mathrm{e}') - \frac{2}{3}\frac{T_\mathrm{e}'^2}{n'}\mathscr{C}'(n') = \Lambda_{T_\mathrm{e}}', \tag{1b}$$

$$\frac{\mathrm{d}\Omega'}{\mathrm{d}t'} - \mathscr{C}'(n'T_\mathrm{e}') = \Lambda_\Omega'. \tag{1c}$$

Here the vorticity, Ω', of the electric drift, the advective derivative, $\mathrm{d}/\mathrm{d}t'$ and the curvature operator, $\mathscr{C}'$ due to the non-uniform magnetic field are respectively defined by

$$\Omega' = \nabla_\perp'^2\phi', \tag{2a}$$

$$\frac{\mathrm{d}}{\mathrm{d}t'} = \frac{\partial}{\partial t'} + \mathbf{v}_E' \cdot \nabla'\phi' = \frac{\partial}{\partial t'} + \frac{1}{B'}\mathbf{b} \times \nabla'\phi' \cdot \nabla', \tag{2b}$$

$$\frac{1}{B'} = 1 + \frac{r_0 + \rho_{s,0}x'}{R_0}, \tag{2c}$$

$$\mathscr{C}' = -\frac{\rho_{s,0}}{R_0}\frac{\partial}{\partial y'}. \tag{2d}$$

All the quantities appearing in the above equations, with the exception of the minor and major radii, r_0 and R_0, are dimensionless and expressed in the *Bohm normalized* form, in which the characteristic temporal and spatial scales are chosen as the ion gyro-frequency, $\omega_{\mathrm{ci},0} = eB_0/m_\mathrm{i}$ and the (hybrid) thermal gyro-radius, $\rho_{s,0} = c_{s,0}/\omega_{\mathrm{ci},0}$. Here $c_{s,0} = (T_{\mathrm{e},0}/m_\mathrm{i})^{1/2}$ is the cold ion plasma sound speed, B_0 is the magnitude of the local magnetic field strength and the zero subscript indicates nominal (dimensional) values, typically chosen at the separatrix (or last closed flux surface, LCFS) location on the outboard mid-plane of the tokamak. Bohm normalization is made explicit in equations (1) and (2) by indicating every normalized quantity with a prime,

$$n' = \frac{n}{n_0}, \qquad T_\mathrm{e}' = \frac{T_\mathrm{e}}{T_{\mathrm{e},0}}, \qquad \phi' = \frac{e\phi}{T_{\mathrm{e},0}}, \tag{3a}$$

$$B' = \frac{B}{B_0}, \qquad t' = t\omega_{\mathrm{ci},0}, \qquad \mathbf{x}' = \frac{\mathbf{x}}{\rho_{s,0}}. \tag{3b}$$

Neglecting the weak spatial variation of the magnetic field strength on the outboard mid-plane, the non-dimensional scales may be approximated by

$$\omega_\mathrm{ci}' = \frac{\omega_\mathrm{ci}}{\omega_{\mathrm{ci},0}} \approx 1, \qquad c_\mathrm{s}' = \frac{c_\mathrm{s}}{c_{s,0}} = T_\mathrm{e}'^{1/2}, \qquad \rho_\mathrm{s}' = \frac{\rho_\mathrm{s}}{\rho_{s,0}} \approx T_\mathrm{e}'^{1/2}. \tag{4}$$

The Λ_a' terms (with $a = n, \Omega, T_\mathrm{e}$) on the right-hand side of equations (1), represent dissipation as a result of perpendicular diffusion due to collisions, $D_{\perp a}'\nabla_\perp'^2 a'$, and parallel losses to the divertor targets, $a'/\tau_{\|a}'$,

$$\Lambda_n' = D_{\perp n}'\nabla_\perp'^2 n' - \frac{n'}{\tau_{\|n}'}, \tag{5a}$$

$$\Lambda_{T_\mathrm{e}}' = D_{\perp T_\mathrm{e}}'\nabla_\perp'^2 T_\mathrm{e}' - \frac{T_\mathrm{e}'}{\tau_{\|T_\mathrm{e}}'}, \tag{5b}$$

$$\Lambda_\Omega' = D_{\perp\Omega}'\nabla_\perp'^2\Omega' - \frac{\Omega'}{\tau_{\|\Omega}'}, \tag{5c}$$

where $D_{\perp a}' = D_{\perp a}/(\rho_{s,0}^2\omega_{\mathrm{ci},0})$ are the perpendicular diffusivities of particles, momentum and electron heat, and $\tau_{\|a}' = \tau_{\|a}\omega_{\mathrm{ci},0}$ are the corresponding parallel loss times. These six

parameters are both necessary and sufficient to close the dynamical system (1), which is then discretized in two spatial dimensions. The computational domain forms a box whose sides have an extent of hundreds of $\rho_{s,0}$. In order to adopt a local slab approximation, the simulation domain is limited to the neighbourhood of the outer mid-plane with the local radial and poloidal coordinates denoted by x' and y' respectively. The resulting code has been named ESEL to emphasize its treatment of *Edge-SOL Electrostatic* turbulence [10–14].

2.2. Sub-sonic advection vs. sheath dissipation

The term $\Omega'/\tau'_{\|\Omega}$, denoting parallel loss of vorticity, deserves a special mention. Elsewhere in the literature [15–20], this term is often replaced by a so-called *sheath dissipation* term, $\phi'/\tau'_{\|\Omega}$, which removes vorticity at a rate proportional to the local electrostatic potential (an extended discussion of electrostatic sheaths may be found in [21] and their role in SOL turbulence dissipation in [22]). The implication of this term is best illustrated by Fourier transforming (1c). In the resulting spectral representation, the gradient operator, $\nabla'_\perp$, is replaced by the perpendicular wave number, $k'_\perp$, and the vorticity, $\Omega' = \nabla'^2_\perp \phi'$ by $-k'^2_\perp \phi'_k$ where ϕ'_k is the amplitude of the k-th mode. Neglecting curvature and collisional diffusion, the linearized evolution equation then implies,

$$\frac{\mathrm{d}\ln\phi'_k}{\mathrm{d}t'} = -\frac{1}{k'^2_\perp \tau'_{\|\Omega}} = -\frac{1}{\tau'_{\|\phi}} \tag{6}$$

As a result, ϕ'_k decays with a time constant, $\tau'_{\|\phi}$ which is proportional to $k'^2_\perp$. Consequently, large perturbations decay faster than smaller ones at the rate proportional to the square of their size.

Comparison of the two-dimensional images in [17–19], where the sheath dissipation term is invoked, with those from ESEL simulations in [11–14], where it is not, demonstrate how this preferential damping of large scales dramatically changes the morphology of turbulent structures (with rounded, drop-like *blobs*, in the absence of sheath dissipation, sharpened into radially protruding *fingers*, when it is present).

Before discussing the relative merits of the two momentum (vorticity) damping terms described above to simulating SOL turbulence in a real tokamak, we define the SOL plasma electron and ion collisionalities (or the inverse *Knudsen* numbers, Kn) as,

$$\nu^*_e \equiv \frac{1}{\mathrm{Kn_e}} \equiv \frac{L_\|}{\lambda_{ee}} = \frac{L_\|}{v_{te}\tau_{ei}} \propto \frac{L_\| n_e}{T^2_e}, \qquad \nu^*_i \equiv \frac{1}{\mathrm{Kn_i}} \equiv \frac{L_\|}{\lambda_{ii}} = \frac{L_\|}{v_{ti}\tau_{ii}} \propto \frac{L_\| n_i}{T^2_i}, \tag{7}$$

where $L_\|$ is the outer mid-plane to target connection length, λ_e and λ_i are the electron and ion collisional mean-free-paths, $v_{te} = (T_e/m_e)^{1/2}$ and $v_{ti} = (T_i/m_i)^{1/2}$ are the electron and ion thermal speeds, and τ_{ei} and τ_{ii} are the electron-ion and ion-ion collisional times, also expressed in terms of collisional frequencies $\nu_{ei} \equiv \tau^{-1}_{ei}$ and $\nu_{ii} \equiv \tau^{-1}_{ii}$, [26–35],

$$\nu_{ei}/Z \equiv (Z\tau_{ei})^{-1} = \nu_{ee} \equiv \tau^{-1}_{ee} \equiv \frac{\sqrt{2}n_e e^4 \ln\Lambda}{12\pi^{3/2}\varepsilon^2_0 m^{1/2}_e T^{3/2}_e}, \tag{8a}$$

$$\nu_{ii} \equiv \tau^{-1}_{ii} \equiv \frac{\sqrt{2}n_i Z^4 e^4 \ln\Lambda}{12\pi^{3/2}\varepsilon^2_0 m^{1/2}_i T^{3/2}_i} = \nu_{ei}\left(\frac{m_e}{m_i}\right)^{1/2}\left(\frac{T_e}{T_i}\right)^{3/2} Z^2, \tag{8b}$$

Neglecting the effect of the magnetic shear in the vicinity of the X-point region, $L_\parallel$ may be estimated as $\pi R_0 q_{95}$, where q_{95} is the safety factor at the 95% poloidal magnetic flux surface. However, in more complicated magnetic geometries, this simple expression may introduce significant errors. For example, in the TCV plasmas discussed in [8–11], magnetic equilibrium reconstruction yields $L_\parallel \approx 15\,\text{m}$ compared with $\pi R_0 q_{95} \approx 9$ m. In addition, $L_\parallel$ in TCV can vary by up to 50% across the SOL region. In what follows, $L_\parallel$ will therefore refer to the equilibrium reconstructed value, with a known radial variation, $L_\parallel = L_\parallel(x')$. Unless otherwise stated, v_e^* will refer to the separatrix values of n_e and T_e, and to the near-SOL value of $L_\parallel$.

In the authors' opinion, the sheath dissipative formulation, although potentially appropriate to *sheath-limited*, collisionless ($v_e^* < 10$) conditions, significantly misrepresents the actual damping mechanism under *conduction-limited*, collisional ($v_e^* > 10$) conditions. The reasons, as outlined in [12–14, 23, 24], include:

- the neglect of parallel gradients,
- field line averaging of non-linear terms,
- inconsistency in the transition region between open and closed field lines.

Since the SOL plasma on TCV and indeed on most other tokamaks, is collisional (in the case of TCV plasmas used for turbulence studies, $v_e^* \approx 50$, see section 3), the advective damping term (5c) used in the ESEL model is likely to be more accurate than its sheath dissipative cousin.

It is instructive to reinforce the above arguments, with a more pragmatic assessment of sheath dissipation. Roughly speaking, one would expect the sheath to influence filament dynamics if, and only if, information has sufficient time to propagate between the outer mid-plane of the torus and the nearest solid surface (i.e. one of the divertor targets), in the time it takes the plasma filament to traverse a radial distance equal to its radial width. We anticipate equation (23) in section 5.1 and approximate the former time as $\tau_\parallel \approx L_\parallel/\xi c_s$ and the latter as $\tau_\perp \approx \Delta x/v_\perp$; here ξc_s is the warm ion sound speed, also given later in equation (15). For the case of the TCV simulations reported in section 6, these times can be evaluated as $\tau_\parallel \approx 300\,\mu\text{s}$ and $\tau_\perp \approx 2\,\text{cm}/2\,\text{km}\,\text{s}^{-1} = 10\,\mu\text{s}$, where we used the a posteriori observation that $\Delta x < 2\,\text{cm}$ and $v_\perp < 2\,\text{km}\,\text{s}^{-1}$ in the TCV relevant ESEL simulations. It is now easy to see why sheath dissipation is inappropriate: the plasma blob enters and leaves any given flux tube so quickly, that the sheath 'finds out' about the pressure perturbation only after the filament has long left the flux tube. Thus, for fundamental reasons of temporal causality, the sheath cannot influence the dynamics of the turbulent filament, whenever

$$\frac{\tau_\perp}{\tau_\parallel} \sim \frac{\Delta x \xi c_s}{L_\parallel v_\perp} \ll 1 \tag{9}$$

which defines the *advective dissipation criterion*; in contrast, sheath dissipation requires $\tau_\parallel/\tau_\perp \sim 1$. Since $\Delta x/L_\parallel \sim \lambda_{\text{SOL}}/L_\parallel \sim 10^{-3}$, $v_\perp \sim 1\,\text{km/s}$ and $v_\perp/\xi c_s < 0.03$ on most tokamaks (these results follow from measurements of radial SOL widths and radial propagation velocities of disturbances in the SOL, respectively), we find $\tau_\parallel/\tau_\perp \sim 30$ such

that equation (9) is indeed satisfied. Evidently, radial motion of turbulent structures is too fast to allow sheath dissipation in the typical tokamak SOL plasma.

It is worth noting that in ITER conduction-limited and partially detached conditions are required to prevent excessive erosion of the divertor target plates [25]. This means that despite low upstream collisionality ($v_e^* \approx 10$), strong parallel gradients are present in the divertor plasma due to the neutral trapping and plasma compression. As a result, the upstream plasma is effectively screened from the sheath by the dense plasma and neutral cloud in the divertor region. On the basis of these considerations, one would likewise not expect the sheath dissipative term to be dominant in the ITER SOL.

2.3. Boundary conditions and radial variation of damping terms

In the TCV study [10, 11] the following boundary conditions were imposed at the innermost (core) and outermost (far-SOL) boundaries,

$$\Omega' = \phi' = T_e' - 1 = n' - 1 = 0 \quad \text{at } x = 0, \tag{10a}$$

$$\Omega' = \frac{\partial \phi'}{\partial x'} = \frac{\partial T_e'}{\partial x'} = \frac{\partial n'}{\partial x'} = 0 \quad \text{at } x = L_x, \tag{10b}$$

with periodic boundary conditions being applied at the upper and lower poloidal limits of the simulation grid. Thus, the turbulence was driven by a pressure gradient in the edge region due to a prescribed particle density and temperature at the inner boundary, which explains the absence of volumetric sources in equations (1a)–(1c).

In addition, the radial variations of $D'_{\perp a}$ and $\tau'_{\parallel a}$ were approximated by

$$D'_{\perp a} = \text{const}, \tag{11}$$

$$\frac{1}{\tau'_{\parallel a}} = \frac{\sigma'_{a,l}}{2} \left[1 + \tanh\left(\frac{x' - x'_l}{\delta'_l}\right)\right] + \frac{\sigma'_{a,w} - \sigma'_{a,l}}{2} \left[1 + \tanh\left(\frac{x' - x'_w}{\delta'_w}\right)\right]$$

where $\sigma'_{a,l}$ and $\sigma'_{a,w}$ are constants representing respectively the strength of parallel losses in the main SOL and the wall shadow, x'_l and x'_w correspond to the radial positions of the LCFS and the last main-SOL flux surface, and δ'_l and δ'_w are the radial widths over which the parallel losses are activated (typically $\delta'_l = \delta'_w = 1$). Note that the same radial profile shape was used for all three fields. The absence of parallel losses for $x' < x'_l - 2\delta'_l$ simulates the region of closed field lines, whereas its presence for $x' > x'_l + 2\delta'_l$, where $\tau'_{\parallel a} = 1/\sigma'_a$ represents the SOL, i.e. the region of open field lines.

Additional information, beyond that contained in the reduced fluid model, is clearly required to determine the magnitude and the functional form of $D'_{\perp a}$ and σ'_a, which explains the simple form of $D'_{\perp a} = \text{const}$ and $\sigma'_a = \text{const}$ used in early SOL turbulence studies [17–20] and in ESEL simulations [10–14]. In the subsequent sections, we derive first principle forms for the desired damping terms based on a judicious combination of neoclassical and classical collisional transport coefficients in the perpendicular and parallel directions, respectively.

3. Energy relaxation times

We begin with a few comments on equations (1)–(4), in which $T_i \ll T_e$ was assumed. The cold ion approximation may at first sight seem inappropriate in the context of SOL plasmas, in which the ions are not only warm ($T_i \sim T_e$), but typically hotter than the electrons, $T_i/T_e \approx 2$ [21, 43]. Nonetheless, it can be readily argued, that this simplification is justified under collisional conditions ($v_e^* \gg 1$), such as those reported in the TCV experiments [8–11],

$$n_0 \approx 10^{19}\,\mathrm{m}^{-3}, \qquad T_{e,0} \approx 20\,\mathrm{eV}, \qquad A = 2Z = 2, \tag{12}$$
$$R_0 \approx 0.9\,\mathrm{m}, \qquad B_0 \approx 1.4\,\mathrm{T}, \qquad q_{95} \approx 3,$$

for which equation (7) yields $v_e^* \approx 30$. The argument is based on the ratios of the collisional energy equipartition time, $\tau_{ie,\varepsilon}$, defined as a characteristic time in which ion and electron temperatures relax to a common value, $\mathrm{d}T_i/\mathrm{d}t = (T_e - T_i)/\tau_{ie,\varepsilon}$, which is larger than the electron-ion collision time, (8a), by twice the mass ratio,

$$v_{ie,\varepsilon} \equiv \tau_{ie,\varepsilon}^{-1} = 2\left(\frac{m_e}{m_i}\right)\left(\frac{n_e}{n_i}\right)v_{ei} = \frac{n_e Z^2 e^4 m_e^{1/2}\ln\Lambda}{3\sqrt{2}\pi^{3/2}\varepsilon_0^2 m_i T_e^{3/2}}, \tag{13}$$

(this expression can be found in most sources, in particular [26–34]; the reader should be aware that reference [35] derives $v_{ie,\varepsilon}$ to be a factor of two larger), the parallel particle loss time, $\tau_{\|n}$, equation (23), and the parallel electron cooling time, $\tau_{\|T_e}$, equation (25) (in the last two instances we again anticipate the results of section 5; the derivation of the ratios in terms of dimensionless parameters can also be found in [22])

$$\frac{\tau_{\|n}}{\tau_{\|Te}} = \frac{2}{3M_\|}\left(\frac{m_i}{m_e}\right)^{1/2}\frac{1}{v_e^*} = \frac{2}{3M_\|}\left(\frac{m_i}{m_e}\right)^{1/2}\mathrm{Kn}_e \tag{14a}$$

$$\frac{\tau_{ie,\varepsilon}}{\tau_{\|n}} \approx \frac{1}{M_\|}\left(\frac{m_i}{m_e}\right)^{1/2}\frac{1}{v_e^*} \approx \frac{1}{M_\|}\left(\frac{m_i}{m_e}\right)^{1/2}\mathrm{Kn}_e \tag{14b}$$

$$\frac{\tau_{ie,\varepsilon}}{\tau_{\|Te}} = \left(\frac{3.2}{1.5}\frac{m_i}{m_e}\right)\frac{1}{v_e^{*2}} = \left(\frac{3.2}{1.5}\frac{m_i}{m_e}\right)\mathrm{Kn}_e^2 \tag{14c}$$

where $M_\|$ is the parallel Mach number, defined as the ratio of the parallel flow velocity, $v_\|$ and the warm ion sound speed, ξc_s,

$$M_\| = \frac{v_\|}{\xi c_s}, \qquad c_s = \sqrt{\frac{T_e}{m_i}}, \qquad \xi = \sqrt{Z + \frac{T_i}{T_e}}. \tag{15}$$

We note that $\tau_{ie,\varepsilon}/\tau_{\|T_e}$ decreases quadratically with collisionality, such that for $v_e^* \gg 1$ equipartition is sufficiently strong to ensure that the electron and ion energies are effectively coupled, $T_i \sim T_e$. For $v_e^* \ll 1$ it plays no role in the energy balance and the ion and electron channels become completely decoupled. The transition between weak and strong coupling occurs at the *equipartition* collisionality, $v_{e,\varepsilon}^*$ (or the *equipartition* Knudsen number, $\mathrm{Kn}_{e,\varepsilon}$),

$$v_{e,\varepsilon}^* = \mathrm{Kn}_{e,\varepsilon}^{-1} = \left(\frac{3.2}{1.5}\frac{m_i}{m_e}\right)^{1/2} \approx 88 \tag{16}$$

which we evaluate for deuterium ions. We infer that for $v_e^* > v_{e,\varepsilon}^*$ the ion and electron channels are sufficiently coupled for heat to be conveyed through the faster channel (that is,

electron conduction parallel to **B** and ion conduction perpendicular to **B**) and then transferred by collisions from the hotter to the colder species (that is, from ions to electrons). As a result, the effective perpendicular electron heat diffusivity consists of a small electron contribution and a much larger ion contribution multiplied by an equipartition factor,

$$\frac{D'_{\perp T_e}}{\chi'_{\perp i}} \approx \frac{\chi'_{\perp e}}{\chi'_{\perp i}} + \Theta_{ie} \approx 2.3 \left(\frac{m_e}{m_i}\right)^{1/2} + \Theta_{ie} \approx 0.038 + \Theta_{ie} \quad (17)$$

where the last expression is evaluated for $A = 2$, $Z = 1$ and Θ_{ie} is given by

$$\Theta_{ie} \equiv \left(1 + \frac{\tau_{ie,\varepsilon}}{\tau_{\|T_e}}\right)^{-1} = \left(1 + \frac{v^*_{e,\varepsilon}}{v^*_e}\right)^{-1} = \left(1 + \frac{\mathrm{Kn}_e}{\mathrm{Kn}_{e,\varepsilon}}\right)^{-1} \quad (18)$$

Note that Θ_{ie} ranges from zero for $v^*_e \ll v^*_{e,\varepsilon}$ to unity for $v^*_e \gg v^*_{e,\varepsilon}$, passing through $\Theta_{ie} = 1/2$ when $v^*_e = v^*_{e,\varepsilon}$. In other words, $D'_{\perp T_e}$ is given by $\chi'_{\perp e}$ in the collisionless limit and by $\chi'_{\perp i}$ in the collisional limit. In the TCV experiment, we find $\Theta_{ie} \approx (1 + 88/30)^{-1} \approx 0.26 \gg 0.038$, such that the ion contribution clearly dominates.

In closing we note that the thermal energy of the ions generates finite Larmor radius corrections to drift fluid dynamics and modifies both perpendicular dissipation and parallel losses. From this perspective, the cold-ion, reduced-fluid model which forms the basis of the ESEL code, is only a crude approximation of actual plasma dynamics, irrespective of the equipartition argument presented above.

4. Perpendicular transport coefficients

We henceforth restrict the discussion to collisional SOL turbulence ($v^*_e > 10$) and assume that radial diffusion of momentum and energy is dominated by the ion channel, that is, by ion-ion collisions. This calls for classical (denoted by lower case c) Bohm normalized expressions for the particle ($D'^c_\perp$), momentum ($\mu'^c_\perp$), ion heat ($\chi'^c_{\perp i}$) and electron heat ($\chi'^c_{\perp e}$) diffusivities [26],

$$D'^c_\perp = \frac{(1+\vartheta)\rho_e^2 v_{ei}}{\rho_{s,0}^2 \omega_{ci,0}} = \frac{(1+\vartheta)\rho_e^2 v_{ei}}{\rho_s^2 \omega_{ci}} \rho_s'^2 \omega'_{ci} = (1+\vartheta)T'_e \frac{v_{ei}}{\omega_{ce}} \propto \frac{n'}{T_e'^{1/2}}, \quad (19a)$$

$$\chi'^c_{\perp i} = \frac{2\rho_i^2 v_{ii}}{\rho_{s,0}^2 \omega_{ci,0}} = \frac{2\rho_i^2 v_{ii}}{\rho_s^2 \omega_{ci}} \rho_s'^2 \omega'_{ci} = 2T'_i \frac{v_{ii}}{\omega_{ci}} \propto \frac{n'}{T_i'^{1/2}}, \quad (19b)$$

$$\chi'^c_{\perp e} = \frac{4.66\rho_e^2 v_{ee}}{\rho_{s,0}^2 \omega_{ci,0}} = \frac{4.66\rho_e^2 v_{ee}}{\rho_s^2 \omega_{ci}} \rho_s'^2 \omega'_{ci} = 4.66T'_e \frac{v_{ee}}{\omega_{ce}} \propto \frac{n'}{T_e'^{1/2}}, \quad (19c)$$

$$\mu'^c_\perp = \left(\frac{\eta_i}{n_i m_i}\right)' \approx \left(\frac{\eta_{1i} + \eta_{2i}}{2n_i m_i}\right)' = \frac{3}{8}\chi'^c_{\perp i} \propto \frac{n'}{T_i'^{1/2}}, \quad (19d)$$

where $T'_i = T_i/T_{i,0}$, $\vartheta \equiv T_i/T_e$, ω_{ce} and ω_{ci} are the electron and ion gyro-frequencies, and η_{1i} and η_{2i} are the dominant components of the viscosity tensor as defined by Braginskii [26]. Note that $D'^c_\perp$ represents the *ambipolar* particle diffusivity, which ensures charge conservation and quasi-neutrality and which is a factor of $(1 + \vartheta)$ larger than the classical electron diffusivity, $\rho_e^2 v_{ei}$.

4.1. Classical perpendicular transport

In a classical, fully ionised plasma, the ion heat and momentum diffusivities are comparable and much larger than the particle and electron heat diffusivities. This is best expressed in terms of dimensionless fluid groups: the Schmidt (Sc), Lewis (Le) and Prandtl (Pr) numbers, which are much larger than unity, with the exception of the ion Prandtl number, which is less than but comparable to one, and the electron Lewis number, which is greater than but comparable to one,

$$\text{Sc}^{\text{c}}_{\perp} \equiv \frac{\mu^{\text{c}}_{\perp}}{D^{\text{c}}_{\perp}} = \frac{3}{4(1+\vartheta)}\left(\frac{m_{\text{i}}}{\vartheta m_{\text{e}}}\right)^{1/2} \approx 25, \tag{20a}$$

$$\text{Le}^{\text{c}}_{\perp\text{i}} \equiv \frac{\chi^{\text{c}}_{\perp\text{i}}}{D^{\text{c}}_{\perp}} = \frac{2}{1+\vartheta}\left(\frac{m_{\text{i}}}{\vartheta m_{\text{e}}}\right)^{1/2} \approx 60, \qquad \text{Le}^{\text{c}}_{\perp\text{e}} \equiv \frac{\chi^{\text{c}}_{\perp\text{e}}}{D^{\text{c}}_{\perp}} \approx 2.5, \tag{20b}$$

$$\text{Pr}^{\text{c}}_{\perp\text{i}} \equiv \frac{\mu^{\text{c}}_{\perp}}{\chi^{\text{c}}_{\perp\text{i}}} = \frac{3}{8}, \qquad\qquad \text{Pr}^{\text{c}}_{\perp\text{e}} \equiv \frac{\mu^{\text{c}}_{\perp}}{\chi^{c}_{\perp\text{e}}} = 0.161\left(\frac{m_{\text{i}}}{\vartheta m_{\text{e}}}\right)^{1/2} \approx 10. \tag{20c}$$

As before all the above expressions have been evaluated for $A = 2$, $Z = 1$ and $\vartheta = 1$. In the context of edge–SOL turbulence simulations, we are particularly interested in the classical viscosity coefficient (or *momentum* diffusivity), $\mu_{\perp}$, which determines the damping of sheared poloidal flows and hence the frequency of intermittent bursts [36–38]. Based on equations (20a) and (20c), we see that $\mu^{\text{c}}_{\perp}$ greatly exceeds $D^{\text{c}}_{\perp}$ and is comparable to $\chi^{\text{c}}_{\perp\text{i}}$. It is worth emphasizing that this comparatively strong viscous damping of poloidal (zonal) flows in the edge–SOL region has not been fully appreciated in the past.

4.2. Neoclassical perpendicular transport

In toroidal plasmas under collisional conditions, the classical expressions (19a)-(19d) are modified by neoclassical, Pfirsch-Schlüter (PS) corrections, which to first order can be approximated as a multiplication by the square of the safety factor, q^2_{95} [39]. However, the derivation of these corrections presupposes the existence of *closed* field lines, or rather closed flux surfaces, and employs flux-surface averaging to obtain the effective radial diffusivities. In contrast, we are interested in the local values of these diffusivities near the outer mid-plane, spanning both the closed and open field line regions. Since a rigorous treatment of neoclassical transport on open field lines is not available in the literature, one is forced to resort to an approximate treatment.

We begin by recalling the basic principles of Pfirsch-Schlüter diffusion, a clear exposition of which may be found in [31], illustrating the key flows in figure 1. One of the hallmarks of confined plasmas is the appearance of diamagnetic, or magnetisation, fluxes which are driven by radial gradients of thermodynamic quantities, e.g. (n, p_e, p_i), and flow on nested flux surfaces in the direction perpendicular to both the magnetic field lines and the flux surface normal, e.g. $\mathbf{b} \times \nabla p$. In a cylindrical geometry, these fluxes have a vanishing divergence, e.g. $\nabla \cdot (\mathbf{b} \times \nabla p) = 0$, and thus do not affect the evolution of thermodynamic quantities. This solenoidal behaviour is broken by the appearance of toroidicity, which leads to a non-vanishing divergence , which can be related to the downward (upward) drift of guiding centres
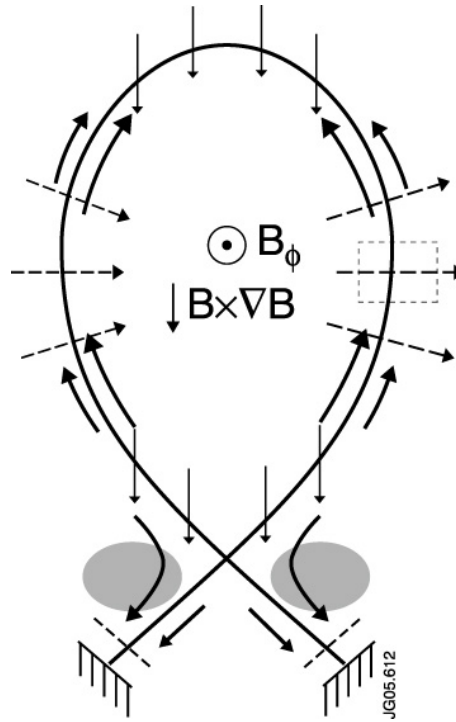
Figure 1. Schematic representation of neoclassical, Pfirsch-Schlüter transport on closed and open flux surfaces, for $\mathbf{B} \times \nabla B$ direction towards the X-point (vertically down). The thin arrows represent downward ion magnetic drifts, the thick arrows the parallel return flows and the dashed arrows the resulting radial transport. The shaded region illustrates the area of strong plasma-neutral interaction and thus increased recycling in the divertor plasma. The location of the magnetic pre-sheath (not to scale) is indicated by the dashed lines adjacent to the divertor targets. Finally, the dotted box represents the poloidal projection of the computational domain (not to scale) used in ESEL simulations.

of the form $\mathbf{B} \times \nabla B$ caused by a non-uniform magnetic field (thin arrows in figure 1). The resulting build up of charge, density or pressure, drives parallel return flows within the flux surface, which largely compensate for the non-solenoidal part of the diamagnetic flux (thick arrows in figure 1). Under collisional conditions ($v_e^* \gg 1$), the parallel friction in these return flows generates a radial flux towards the centre (inward) on the high field side and away from the centre (outward) on the low field side of the torus (dashed arrows in figure 1). For a high aspect ratio flux surface ($R_0/r \gg 1$), these fluxes have an approximately sinusoidal poloidal dependance, namely $q_r^{PS} \propto q_{95}^2(1 + (R_0/r)\cos\theta)$, where $\theta = 0$ at the outer mid-plane. Performing a flux surface average leaves a net outward flux which is smaller than the low and high field side fluxes by roughly the small factor r/R_0. This average radial flux, known as the Pfirsch-Schlüter flux, is proportional to some average radial thermodynamic gradient and thus acts to relax this gradient. The process is generally known as neoclassical Pfirsch-Schlüter diffusion.

The extension of the above analysis to the problem of calculating local diffusivities in the ESEL computational domain (dotted box in figure 1) poses two separate problems. First, it makes the problem local to the outer mid-plane of the tokamak. The already mentioned

poloidal dependance, $q_r^{PS}(\theta) \propto q_{95}^2(1 + (R_0/r)\cos\theta)$, means that the local radial flux near the outer mid-plane is larger than the flux surface average radial flux roughly by a factor $R_0/r \approx 3$. Second, it introduces the effect of open field lines on either side of the X-point. These may be viewed as volumetric sinks of particles, pressure or charge (in fact the sink occurs by parallel loss to the nearby divertor plates), and will tend to counteract the build up of these quantities in the neighbourhood of the X-point, as discussed in the previous paragraph. Since it is this build up which drives parallel return flows in the upstream SOL, we may expect these upward flows and the associated radial PS flux to be reduced by some unknown factor related to the parallel profiles of the thermodynamic quantity in question. we approximate this factor as the ratio of the parallel distance upstream of the X-point, $L_\parallel^{X-X}$, and the sum of the parallel distances between the X-point and inner and outer targets, $L_\parallel^{i-X} + L_\parallel^{o-X}$, which for large aspect ratio tokamaks is comparable to R_0/r. We thus find that the effects of locality tend to to increase, and those of topology to reduce, the radial fluxes by comparable factors, such that the two effects roughly compensate.

Bearing in mind the above remarks, we henceforth employ the actual PS expressions for the particle and momentum diffusivities, $D'_{\perp n}$ and $D'_{\perp \Omega}$, and follow the approach laid out in equations (17)–(18) to construct an effective heat diffusivity, $D'_{\perp T_e}$,

$$D_{\perp n}^{\prime PS} = (1 + 1.3q_{95}^2)D_\perp^{\prime c}, \tag{21a}$$

$$D_{\perp T_e}^{\prime PS} \approx \chi_{\perp e}^{\prime PS} + \Theta_{ie}\chi_{\perp i}^{\prime PS}, \qquad \chi_{\perp e}^{\prime PS} = (1 + 1.6q_{95}^2)\chi_{\perp e}^{\prime c}, \tag{21b}$$

$$D_{\perp \Omega}^{\prime PS} = \mu_{\perp i}^{\prime PS} \approx \frac{3}{8}\chi_{\perp i}^{\prime PS}, \qquad \chi_{\perp i}^{\prime PS} = (1 + 1.6q_{95}^2)\chi_{\perp i}^{\prime c}. \tag{21c}$$

The subscript T_e is retained to emphasize the use of $D'_{\perp T_e}$ in the electron energy equation (1b). As previously mentioned, in the strongly collisional limit, the ion and electron channels become thermally coupled ($\Theta_{ie} \to 1$) such that electron heat diffuses radially almost exclusively due to diffusion of ion heat, $D_{\perp T_e}^{\prime PS} \to \chi_{\perp i}^{\prime PS}$. Note that Θ_{ie} does not enter into the viscosity coefficient since plasma momentum is already dominated by the heavier ion species. It is also absent from the particle diffusivity, where electron-ion collisions, which alone lead to particle diffusion, enter through the electron dominated collision frequency. In other words, the degree of collisional coupling between the electron and ion species has little impact on perpendicular particle and momentum diffusion, but dominates the effective diffusion of electron heat.

The dimensionless fluid groups associated with equations (21a)–(21c), now become

$$Sc_\perp^{PS} \equiv \frac{D_{\perp \Omega}^{PS}}{D_{\perp n}^{PS}} \approx \frac{5}{4}Sc_\perp^c \approx 30, \tag{22a}$$

$$Le_\perp^{PS} \equiv \frac{D_{\perp T_e}^{PS}}{D_{\perp n}^{PS}} \approx \frac{5}{4}(Le_{\perp e}^c + \Theta_{ie}Le_{\perp i}^c) \approx 40, \tag{22b}$$

$$Pr_\perp^{PS} \equiv \frac{D_{\perp \Omega}^{PS}}{D_{\perp T_e}^{PS}} = \frac{Sc_\perp^{PS}}{Le_\perp^{PS}} = \frac{Sc_\perp^c}{Le_{\perp e}^c + \Theta_{ie}Le_{\perp i}^c} \approx 0.75, \tag{22c}$$

Once again all expressions are evaluated for $A = 2$, $Z = 1$, $\vartheta = 1$, with the additional assumption of moderate ion-electron coupling, $\Theta_{ie} = 0.5$. Comparison with equations

(20*a*)–(20*c*) reveals that introduction of toroidicity has little effect on the dimensionless fluid groups, i.e. the effective Prandtl number is once again comparable to unity, while the Schmidt and Lewis numbers are much larger than one. As a result, we expect strong viscous damping of poloidal flows in the edge–SOL region and thus reduction of the velocity shear associated with these flows. Since such velocity shear acts to destroy large structures and de-correlate local fluctuations (i.e. acts to suppress turbulent transport), viscous damping of poloidal flows increases the rate at which turbulence can re-establish itself the edge–SOL region. This manifests itself as intermittent (sporadic) enhancements of edge transport, which are accompanied by profile relaxations and ejection of plasma filaments into the SOL [12–14, 36–38].

5. Parallel transport coefficients

We divide the discussion below into parallel transport under steady-state and transient conditions. The former provides a useful starting point for investigating transient particle, momentum and heat propagation, which is required in the context of the present study.

5.1. Steady-state parallel transport

Parallel loss times of particles and electron energy to the divertor have been derived on several occasions under steady-state, *quiescent* SOL plasma conditions [21, 40]. The simplest case is the so-called *simple* SOL in which the net particle source comes not from recycling at the divertor targets, but from net radial influx in the upstream region. Below we present the parallel loss times for such a steady-state, upstream fuelled, simple SOL.

The parallel particle density loss time is easily found as

$$\tau_{\|n} = \frac{L_{\|n}}{v_{\|}} \approx \frac{L_{\|}}{M_{\|}\xi c_{s}}, \qquad \tau'_{\|n} = \tau_{\|n}\omega_{ci} \propto \frac{1}{(\xi T'_{e})^{1/2}}, \tag{23}$$

where $L_{\|n} \equiv 1/|\nabla_{\|}\ln n|$ is the length scale of parallel particle density variation, which in the simple SOL case is comparable to the connection length, $L_{\|}$. Consequently, the Bohm normalized parallel advection loss rate, $1/\tau'_{\|n} \propto (\xi T'_{e})^{1/2}$, decreases as the plasma cools. Determination of the Mach number in equation (23) deserves a comment. It is easily shown that the steady-state balance of mass and momentum requires the flow velocity into the sheath adjacent to the solid (divertor) target to be sonic or supersonic, $M_{\|sheath} \geq 1$ [21]. This is the fluid version of the celebrated *Bohm criterion*. Momentum conservation also requires the particle density at the entrance into the target sheath, n_{t}, to be half the value of the upstream particle density, n_{u}. The particle density loss time can thus be calculated as the ratio of the total flux tube particle content, which can be approximated as $n_{u}L_{\|}$, and the flow rate into the sheath, $n_{t}\xi c_{s}$, with the result $\tau_{\|n} = L_{\|}/(0.5\xi c_{s})$, i.e. $M_{\|} \approx 0.5$ [21]. Similar values follow from more sophisticated calculations, including the analysis of the SOL-average Mach number for different transport assumptions [21]. Invariably we find $M_{\|} \approx 0.5$ under simple SOL conditions. The associated loss mechanism of particles, and any other passive scalar carried by the flow, can be labeled as *sub-sonic advection*.

Electron heat is lost to the divertor due to a combination of sub-sonic advection (or convection) and electron heat diffusion (or conduction). The ratio of these loss mechanisms is given by equation (14a), which predicts that heat diffusion dominates for low-to-moderate collisionalities ($v_e^* < 20$ for A = 2 and $M_\parallel = 0.5$). This roughly corresponds to the *sheath limited* regime ($v_e^* < 10$), in which the Spitzer-Härm (SH) expression for the electron heat diffusivity, $\chi_{\parallel e}^{SH} = 3.2 v_{te}^2 \tau_{ee}$ [41] must be modified by appropriate long mean-free-path corrections or *heat flux limits* (see [42] for a review of heat flux limits in SOL dynamics). In plasma fluid codes, this is typically done by replacing $\chi_{\parallel e}^{SH}$ by a harmonic average form valid under all SOL collisionality regimes,

$$\chi_{\parallel e} = \chi_{\parallel e}^{SH} \left(1 + \frac{3.2}{v_e^* \alpha_e^{FS}} \right)^{-1} \tag{24}$$

The choice of the flux limiting factor, α_e, merits a short comment. One possibility is to evaluate this factor at the free streaming (FS) value $\alpha_e^{FS} \approx 0.8$ [42], which is clearly appropriate to fluid codes, where the effect of the sheath is imposed as a boundary condition. The resulting kinetic correction is typically small in the main SOL (e.g. in the TCV experiments $4/v_e^* < 0.1$), but might be required in the limiter, or wall, shadow region, where $L_\parallel$ is typically reduced by a factor of ten, such that $4/v_e^* \approx 1$. However, it could be argued that for a loss time treatment of parallel losses, the sheath limited value of the flux limiting factor, $\alpha_e^{sheath} \approx 0.07$, is more appropriate (this value is obtained from kinetic calculation of the sheath energy transmission coefficient, $\gamma_e \equiv (Q_e/n v_\parallel T_e)_{sheath} \approx 5$, where Q_e is the electron energy flux into the sheath). The resulting kinetic correction is no longer negligible even in the main SOL (e.g. in the TCV experiments $45/v_e^* \approx 1$). However, due to the arguments in section 5.2, the appropriateness of this sheath expression might equally be questioned. Below, we select the larger value as the default choice of α_e, and discuss the sheath limited value only in the context of parametric variation.

In the collisional limit ($v_e^* \gg 20$), parallel conduction is sharply reduced, and sub-sonic advection becomes dominant. In this limit, the Spitzer-Härm expression may be used without long mean-free-path corrections. The resulting expression for the net energy loss time was derived in [22]. In the present case, we need only consider the electron cooling time $\tau_{\parallel T_e}$, since the interchange model equations (1) are written in terms of the electron temperature and not pressure. This is easily found by assuming parallel diffusion of heat,

$$\tau_{\parallel T_e} = \frac{3}{2} \frac{L_{\parallel T_e}^2}{\chi_{\parallel e}} \approx \frac{3}{2} \frac{L_\parallel^2}{\chi_{\parallel e}^{SH}}, \qquad \tau_{\parallel T_e}' = \tau_{\parallel T_e} \omega_{ci} \propto \frac{n'}{T_e'^{5/2}} \tag{25}$$

Here, as before, we assume $1/L_{\parallel T_e} \equiv |\nabla_\parallel \ln T_e| \approx 1/L_\parallel$, which is appropriate for the upstream fuelled, simple SOL. The conductive cooling rate, $1/\tau_{\parallel T_e}' \propto T_e'^{5/2}/n'$, is a strong function of the electron temperature and is inversely proportional to the particle density. As the SOL plasma cools, this rate decreases sharply, although the reduction is partly offset by the accompanying effect of rarefication (reduction of particle density). Since both the particle and energy removal times, equations (23) and (25), are positive definite, the governing equations (1a)-(1b) and (5a)-(5b) imply that (time-averaged) n' and T_e' decay exponentially with radial distance

away from the separatrix. Moreover, based on (14*a*), T_e' decays faster than n' provided,

$$v_e^* < \frac{2}{3M_\parallel} \left(\frac{m_i}{m_e} \right)^{1/2} \approx 80 \qquad (26)$$

where the expression has been evaluated for $A = 2$, $Z = 1$ and $M_\parallel = 0.5$. Since $v_e^* \approx 30 < 80$ in the TCV experiment, we expect T_e' and n' to decay with comparable e-folding lengths. The above prediction has been verified by solving the evolution equations for n', T_e' and T_i' directly, assuming the profiles are generated by filaments propagating at constant radial velocities [43].

The *simple* SOL expressions obtained above become inaccurate under *high recycling* SOL conditions, when the dominant particle source is the recycling of neutrals in the divertor rather than the perpendicular plasma transport in the upstream region. As a consequence, $L_{\parallel n}$ becomes comparable to the ionisation mean-free-path of neutrals and the approximation $L_\parallel \approx L_{\parallel n}$, used in formulating the parallel particle density loss time in equation (23), is violated. In addition, significant near-target particle density gradients imply that the zero-dimensional description of parallel dynamics, characterised by the parallel loss times, ceases to be useful and a one-dimensional description of parallel dynamics (or a three dimensional description of the whole problem) becomes necessary. On the other hand, the parallel loss time description is well suited to a range of plasma transients in which both particles and energy are ejected into the upstream SOL, as assumed in the simple SOL ansatz. In short, it is just the tool we need for quantifying damping rates due to parallel losses in an edge–SOL turbulence code such as ESEL.

5.2. Transient parallel transport

In the context of the present study, we require the damping rates of turbulent SOL quantities (n', T_e' and Ω') due to parallel losses to the divertor targets. In this regard, the results of the previous section appear of little relevance, as they pertain to *steady-state* (time-independent) conditions, rather than to *transient* (time-dependent) conditions characteristic of SOL turbulence. Despite these differences, the steady-state, simple SOL and the time-dependent, turbulent SOL have one important common feature: both are fuelled by radial transport of particles, momentum and heat in the upstream region. In interchange turbulence, this fuelling is only active on the side of unfavourable magnetic curvature, $\nabla p \cdot \mathbf{b} \cdot \nabla \mathbf{b} > 0$, i.e. the outer mid-plane of the torus, giving rise to the well known ballooning character of the outward fluxes. The resulting relative fluctuations in the turbulent SOL are so large (of order unity) and the radial influx/outflux into any given flux tube so rapid (compared to sonic transit time to divertor targets) as to dominate the transient parallel dynamics, reducing the recycling pattern in the divertor, and the sheath at the target, to the order of secondary effects. In other words, each turbulent eddy (or filament) transiently resembles the simple SOL in so far as it is fueled entirely by radial influx in the upstream region. The difference lies in the parallel gradient scale length applicable in the two case, which may be much smaller than the connection length for the turbulent eddy, $L_{\parallel n} < L_\parallel$. Unfortunately, it is difficult to estimate the relationship between the two lengths without recourse to three dimensional simulations, although one might speculate that $L_{\parallel n}/L_\parallel$ should scale linearly with the initial parallel extent

of the eddy and inversely with the strength of the perturbation, $\tilde{n}/n$, and with the local plasma collisionality. In the absence of such simulations, we can only be guided by experimental results, which indicate that parallel correlation lengths of SOL turbulence (on JET) are indeed comparable to $L_\parallel$, typically $L_{\parallel n} \sim (r/R_0)L_\parallel$, i.e. that SOL turbulence structures take the form of field-aligned plasma filaments [45]. Consequently, we will tentatively apply equations (23) and (25) to turbulent eddies, with the understanding that the resulting parallel loss times (rates) could be overestimated (underestimated) by a factor of order R_0/r. This approach was previously used in [22] to study the dissipative properties of SOL turbulence.

In addition to the uncertainty in $L_{\parallel n}$, the determination of the Mach number in equation (23) is also problematic. In the simple SOL, $M_\parallel$ was derived from the steady-state balance of SOL inventory and parallel outflux. This approach is clearly not relevant to the transient SOL, i.e. to the turbulent eddy. Instead, we must examine the transient parallel flow in response to the parallel pressure gradients in the filament. Such parallel gradients are a direct consequence of the ballooning nature of the interchange motion, which in the electrostatic approximation leads to radial outflow (due to $\mathbf{E} \times \mathbf{B}$ drifts) of hot plasma blobs on the low field side of the torus which transiently increase the local particle density and temperature in any given flux tube as they drift in and out of a succession of flux tubes. The resulting parallel response can be found by solving the particle and parallel momentum conservation laws,

$$\frac{\partial}{\partial t}n + \nabla_\parallel n\mathrm{v}_\parallel \approx S_n \qquad \frac{\partial}{\partial t}(\rho\mathrm{v}_\parallel) + \nabla_\parallel(p + \rho\mathrm{v}_\parallel^2) \approx S_p \qquad (27)$$

where $\rho \approx m_i n$ is the mass density, $p = p_\mathrm{e} + p_\mathrm{i} = n(T_\mathrm{e} + T_\mathrm{i})$ is the total pressure and S_n and S_p are net sources of particles and parallel momentum (note that the effect of warm ions is included explicitly). Rewriting (27) in Lagrangian form, with a parallel convective derivative $\mathrm{d}/\mathrm{d}t \equiv \partial/\partial t + \mathrm{v}_\parallel \nabla_\parallel$, and assuming the sources to be small, as appropriate to the transient, simple SOL, we obtain

$$\frac{\mathrm{d}}{\mathrm{d}t}n + n\nabla_\parallel \mathrm{v}_\parallel \approx 0 \qquad \frac{\mathrm{d}}{\mathrm{d}t}(\rho\mathrm{v}_\parallel) + \nabla_\parallel p \approx 0 \qquad (28)$$

The above equations represent *acoustic response* to pressure perturbations, in which these propagate parallel to $\mathbf{B}$ with a group velocity equal to the (warm ion) plasma sound speed, ξc_s, equation (15), such that $M_\parallel \approx 1$. In the cold ion approximation, p_i disappears from (28) such that $\xi = 1$ and ξc_s reduces to c_s. In reality, we expect the Mach number to be reduced from the sonic value of unity due to several factors:

- the ambient SOL and divertor plasma pressures, p_{SOL}, reduce $\nabla_\parallel p$, which may be estimated as $\nabla_\parallel p \approx |p - p_{SOL}|/L_\parallel$.
- parallel gyro-viscosity, which should be included in equation (28), would reduce the parallel acceleration,
- kinetic effects tend to reduce the expected $M_\parallel$; for instance one-directional kinetic effusion for $A = 2$, $Z = 1$ and $\vartheta = 1$, predicts $M_\parallel \approx 0.28$, [43, 46].

In view of the above, we expect the transient response to take the form of *sub-sonic*, rather than *sonic*, advection. Below, we adopt $M_\parallel \approx 0.5$ as the nominal Mach number to be used in transient parallel loss expressions. The accuracy of this estimate is clearly the weakest

link in our analysis chain, although the neglect of other effects (impurities, neutrals, finite Larmor radius effects, etc.) should also be noted. A conservative error bar of $\pm 30\%$ should be associated with the suggested $M_\parallel$ value.

The expressions for transient losses of momentum and heat follow by analogy with the previous section. Thus, the parallel cooling time of a filament is given by (25), in which heat flux limits should in general be included. The parallel loss time of vorticity can be approximated by neglecting parallel viscosity, such that perpendicular momentum is removed only by sub-sonic advection. This assumption leads to the simple estimate $\tau'_{\parallel\Omega} \approx \tau'_{\parallel n}$ in which the vorticity is locally damped due to parallel losses. Below, we summarize the final expressions in Bohm normalised form,

$$\tau'_{\parallel\Omega} = \tau'_{\parallel n} \approx \frac{L_{\parallel n}\omega_{\text{ci},0}}{M_\parallel \xi c_s}, \qquad \tau'_{\parallel T_e} = \frac{3}{2}\frac{L^2_{\parallel T_e}\omega_{\text{ci},0}}{\chi_{\parallel e}} \tag{29a}$$

$$M_\parallel \approx 0.5 \qquad\qquad L_{\parallel n} \approx L_{\parallel T_e} \approx L_\parallel \tag{29b}$$

To prevent discontinuities between the region of closed and open field lines, equations (23) and (25) should be combined with the multiple tanh expressions in (11). In other words, parallel losses are activated at the edge–SOL and SOL–wall shadow boundaries with a characteristic radial length scale of one ion gyro-radius ($\delta'_l \approx \delta'_w \approx 1$). With this in mind, the inverse removal times, $1/\tau'_a$, from equations (23) and (25) provide expressions for $\sigma'_{a,l}$ and $\sigma'_{a,w}$ in equation (11).

As a final comment, we observe that parallel losses of both particles, equation (23), and energy, equation (25), which scale as $T'^{1/2}_e$ and $T'^{5/2}_e/n'$, respectively, become progressively weaker as we move outwards away from the separatrix. This translates into longer e-folding lengths in the far-SOL region, which might be interpreted as flattening of the n' and T'_e profiles. According to the above expressions, the degree of profile broadening should increase strongly with SOL collisionality. These features correlate quite well with the degree of profile broadening and its relation to plasma collisionality observed on many tokamaks [47, 49–52].

6. Comparison between ESEL simulations and experimental data from TCV and JET

6.1. Comparison with TCV probe data in Ohmic and L-mode plasmas

We are now ready to predict the required SOL damping coefficients appropriate to the TCV experiments [11]. Evaluating the first principles expressions derived in the previous sections at the nominal separatrix conditions given by equation (12), we find the following values of the radial diffusivities, equations (21a)–(21c),

$$D'^{\text{PS}}_{\perp n} \approx 9 \times 10^{-4}, \qquad D'^{\text{PS}}_{\perp T_e} \approx 1.0 \times 10^{-2}, \qquad D'^{\text{PS}}_{\perp\Omega} \approx 2.5 \times 10^{-2}. \tag{30}$$

and the parallel damping rates, equations (23)–(25),

$$\sigma'_n = \sigma'_\Omega \approx 3.1 \times 10^{-5}, \qquad \sigma'_{T_e} \approx 6\sigma'_n \approx 1.8 \times 10^{-4}, \tag{31}$$

Due to a relatively high collisionality of the TCV SOL plasma, the electron heat diffusivity were evaluated without any recourse to a flux limiting factor. The above coefficients were

taken to be uniform in the main SOL. In the wall shadow region, parallel connection length are shorter than in the main SOL and the parallel damping rates were adjusted accordingly.

Using the values recommended in equations (30) and (31) (with the exception of larger value of $D'_{\perp n} \approx 4.5 \times 10^{-3}$ imposed by numerical constraints) ESEL simulations produce good overall agreement with experimental data [11]. Code and experiment are particularly well matched in terms of the following observables:

- radial profiles of time-averaged particle density, relative particle density fluctuations and their statistical skewness and kurtosis,
- radial profiles of time-averaged radial particle flux, relative particle flux fluctuations, their statistical skewness and kurtosis,
- radial profile of the auto-correlation time and the conditionally averaged pulse waveform shape in the far-SOL
- probability distribution functions of particle density and radial particle flux fluctuations throughout the SOL.

This agreement deteriorates noticeably for factor of two-three departures of the damping rates away from their predicted values, confirming the appropriateness of the reduced fluid, cold-ion approximation with the damping expressions derived here.

At this point, one might raise a valid objection that $D'_{\perp a}$ and σ'_a used in the simulations were assumed to be constant across the SOL, whereas $D'_{\perp a}$ and $\tau'_{\parallel a}$ derived in sections 4 and 5 depend on local values of n' and T'_e, and would thus clearly vary across the SOL. As such, the observed agreement between code and experiment could be considered fortuitous to some extent. This objection may be countered by two separate observations. First and foremost, we note that the values of $D'_{\perp a}$ and σ'_a used in the simulations are evaluated with separatrix values of n' and T'_e, i.e. with $n'(x'_{\text{sep}})$ and $T'_e(x'_{\text{sep}})$, and that the strongly-sheared near-SOL region largely determines the SOL turbulent dynamics. For example, the frequency of intermittent events is linked to the damping of poloidal flow in the edge region and hence to the value of the perpendicular viscosity at the separatrix.

Secondly, as already mentioned, we expect $T'_e(x')$ to decay with an e-folding length equal to (or shorter than) that for $n'(x')$ [55]. Thus, the product $n'/T'^{1/2}_e$ which determines the change of neoclassical diffusivities (21a)–(21c) decays slower than either $n'(x')$ or $T'_e(x')$ (it remains constant when $T'_e(x') \propto n'(x')^2$). This prediction is confirmed by numerical solution of the temporal decay of n', T'_e and T'_i due to parallel losses in the frame of reference moving with the filament [43]. The results indicate that $n'/T'^{1/2}_e$ and $n'/T'^{1/2}_i$ vary by less than 30% for up to three particle density removal times, $0 < t < \tau_{\parallel n}$, which in the TCV experiments are sufficient for the turbulent filament to cross the entire SOL region (excluding the wall shadow). This result was also observed based on averaged values of n' and T'_e obtained using ESEL simulations for both TCV and JET relevant conditions, where $\langle n' \rangle / \langle T'_e \rangle^{1/2}$ was found to remain roughly constant (within 20%) across the edge-SOL region, i.e. in the entire the computational domain, excluding the wall shadow; here $\langle \cdot \rangle$ denotes a spatio-temporal average. More refined simulations, including the spatial variation of $D'_{\perp a}$ and $\tau'_{\parallel a}$ are planned to determine the validity of the above conclusions.

It is also worth noting that the preliminary ESEL simulations, reported in [10], assumed $D'_{\perp n} = D'_{\perp T_e}$. The particle diffusivity was reduced relative to the heat diffusivity in the subsequent simulations, reported in [11], following the derivation of the neoclassical damping terms described here. For reasons of numerical expediency (the required numerical resolution becomes very demanding for realistic values of the particle diffusivity, preventing sufficiently long integration times), only a factor of ten reduction could be implemented into ESEL. However, this level of reduction is sufficient to improve the already good agreement between simulated and TCV-measured turbulence statistics. We note that this agreement justifies *a posteriori* our simple SOL assumptions concerning the parallel flow velocity ($M_\parallel \approx 0.5$) and the parallel scale lengths ($L_{\parallel n} \approx L_{\parallel T_e} \approx L_\parallel$), as least under TCV conditions.

6.2. Comparison with JET probe data in Ohmic and L-mode plasmas

To examine the scaling of ESEL predictions with machine size and related parameters, such as plasma collisionality, we next consider Ohmic and L-mode discharges on the JET tokamak, whose major radius is roughly three times larger than that of TCV. The typical parameters required for the ESEL simulations are taken from a study of SOL radial profiles under Ohmic and L-mode conditions in JET [50]. These are

$$n_0 \approx 10^{19}\,\mathrm{m}^{-3}, \qquad T_{e,0} \approx 45\,\mathrm{eV}, \qquad\qquad T_{i,0} \approx 80\,\mathrm{eV}, \tag{32}$$

$$R_0 \approx 3\,\mathrm{m}, \qquad\qquad B_0 \approx \frac{3}{4}B_{axis} \approx 1.5\,\mathrm{T}, \qquad q_{95} \approx 2.7,$$

for which $\rho_{s,0} = 0.645$ mm, $\omega_{ci,0} = 7.2 \times 10^{-7} s^{-1}$ and $\rho_{s,0}^2 \omega_{ci,0} = 30.0$ m²/s. Applying equations (21*a*)–(21*c*) one finds

$$D'^{PS}_{\perp n} \approx 2.3 \times 10^{-4}, \qquad D'^{PS}_{\perp T_e} \approx 1.25 \times 10^{-3}, \qquad D'^{PS}_{\perp \Omega} \approx 3.3 \times 10^{-3} \tag{33}$$

The above values include the correction due to $\Theta_{ie} = 0.11$, which indicates that the JET Ohmic and L-mode plasmas are somewhat less collisional than those in TCV discharges discussed earlier. Similarly, equations (23)–(25) with $L_\parallel = \pi R_0 q_{95} \approx 25.5$ m, $v_e^* \approx 10$ and $M_\parallel = 0.5$ yield

$$\sigma'_n = \sigma'_\Omega \approx 2.1 \times 10^{-5}, \qquad \sigma'_{T_e} \approx 8.5 \sigma'_n \approx 1.8 \times 10^{-4}, \tag{34}$$

In the JET simulations, the σ's were allowed to vary in response to changes to local particle density and temperature, and were thus functions of position (the D's were held constant everywhere in the computational domain).

To give an indication of the phenomenology of the turbulence emerging from the ESEL simulation for typical JET Ohmic and L-mode conditions, as given by equation (32), instantenous two dimensional mappings of particle density and temperature are shown in figure 2, and should be compared with similar mappings shown in [11]. The computational box, which measures $150\rho_s$ in radial extent and $75\rho_s$ in poloidal extent, is located on the outer mid-plane; the magnetic field is perpendicular to the page. Note the clear breaks in n and T_e between the edge, SOL and wall (limiter) shadow regions. The near-SOL filaments are visibly smaller than those observed in ESEL simulations of TCV plasmas [11], a result of smaller damping coefficients, especially the transverse viscosity, $D'^{PS}_{\perp \Omega}$.
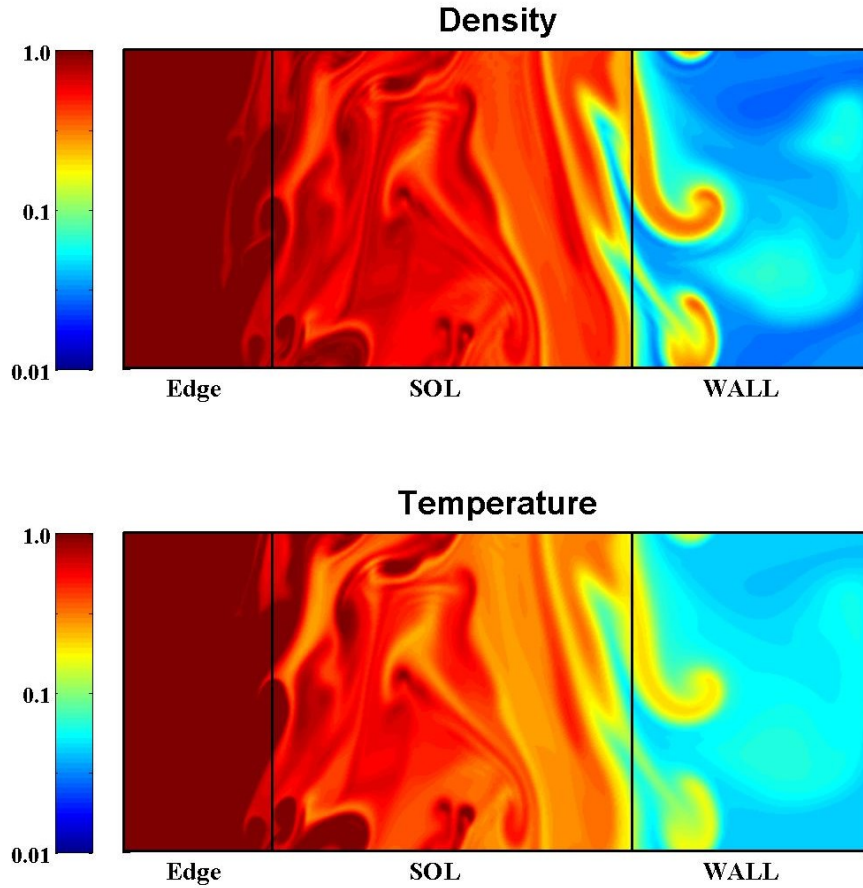
Density

Temperature

Figure 2. Snapshots of two dimensional distribution of particle density and temperature predicted by an ESEL simulation for typical JET Ohmic conditions as given by equation (32). The computational domain is located near the outer mid-plane of the torus and encompasses the edge, SOL and the wall (limiter) shadow regions. The edge region corresponds to 0-25 mm inboard of the separatrix, the SOL to 0-60 mm outboard of the separatrix, and the limiter shadow to 60-100 mm.

To obtain steady-state radial profiles of particle density and electron temperature, the two dimensional mappings of these quantities, figure 2, are averaged in time and in the poloidal variable y', with the resulting $n(r)$ and $T_e(r)$ profiles plotted in the top two frames in figure 3. Also shown in these frames are experimental values of n and T_e measured on JET using the fast reciprocating probe and the Li-beam diagnostics for plasma conditions comparable to (32) at two different upstream densities, see figures 3 and 9 of [50]. Considering the simplified nature of the ESEL simulations, the predicted and measured profiles agree reasonably well, although the agreement is visibly worse for the particle density profile, especially in the far-SOL where the predicted profile is much flatter than observed in the experiment (possible causes of this discrepancy are discussed at the end of the section). The exponential e-folding lengths of $n(r)$ and $T_e(r)$ profiles are shown in the bottom frame of figure 3. Both profiles are steepest in the edge and near-SOL regions, with minimum e-folding lengths of $\lambda_n^{\text{near-SOL}} \approx 20$ mm and
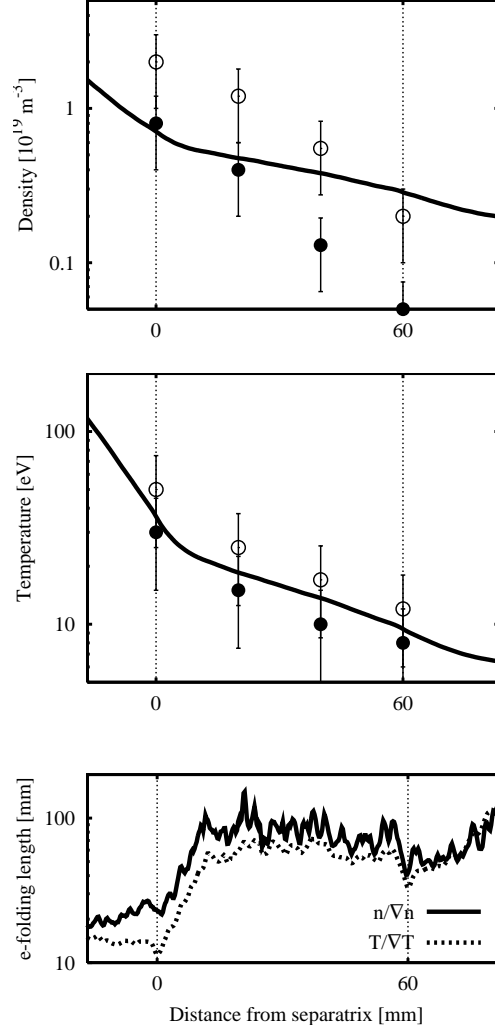
Figure 3. Radial profiles (averaged in time and poloidal direction) of particle density and temperature (top frames), and their radial e-folding lengths (bottom frame), predicted by ESEL for typical JET Ohmic conditions as given by equation (32). Also shown are two sets of experimental profiles for low and high upstream densities, measured on JET using the reciprocating probe and Li-beam diagnostics for Ohmic plasma conditions comparable to (32), see figures 3 and 9 of [50]. The SOL region corresponds to 0-60 mm outboard of the separatrix, and the limiter shadow to 60-100 mm.

$\lambda_{\mathrm{Te}}^{\mathrm{near-SOL}} \approx 10$ mm, and become progressively broader as one moves further into the SOL, $\lambda_{\mathrm{n}}^{\mathrm{far-SOL}} \approx 80$ mm and $\lambda_{\mathrm{Te}}^{\mathrm{far-SOL}} \approx 60$ mm; the averaged (radially across the SOL) e-folding lengths are found as $\lambda_{\mathrm{n}}^{\mathrm{SOL}} \approx 66$ mm and $\lambda_{\mathrm{Te}}^{\mathrm{SOL}} \approx 44$ mm, respectively. The above values compare reasonably well (with the exception of $\lambda_{\mathrm{n}}^{\mathrm{far-SOL}}$) with measured e-folding lengths, again see figures 3 and 9 of [50], which are found as $\lambda_{\mathrm{n}}^{\mathrm{near-SOL}} \approx 20$ mm, $\lambda_{\mathrm{Te}}^{\mathrm{near-SOL}} \approx 10$ mm in the near-SOL, and $\lambda_{\mathrm{n}}^{\mathrm{far-SOL}} \approx 25$ mm, $\lambda_{\mathrm{Te}}^{\mathrm{far-SOL}} \approx 50$ mm in the far-SOL. In particular, both near-SOL lengths are reproduced quite well, whereas the far-SOL particle density length is overestimated by roughly a factor of three.

It is worth noting that the appearance of the double exponential feature in the $n(r)$ and $T_{\mathrm{e}}(r)$ profiles is related to the size of the turbulent structures, as they protrude beyond the
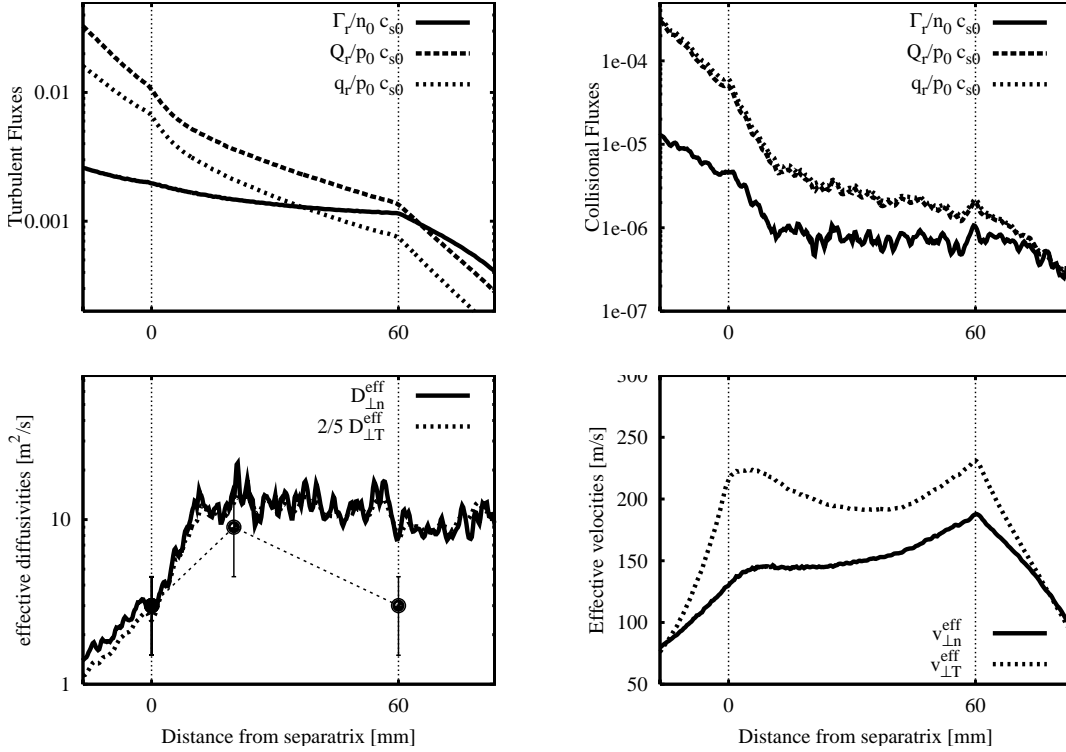
Figure 4. Radial profiles (averaged in time and poloidal direction) of turbulent and collisional (Pfirsch-Schlüter) radial fluxes of particles and energy (top frames) and effective diffusivities and velocities of particles and heat (bottom frames) predicted by ESEL for typical JET Ohmic conditions as given by equation (32). The effective outer mid-plane diffusivity profile inferred from EDGE2D modeling are indicated by solid points with vertical error bars (note that $D_{\perp T}^{\text{eff}} = 2D_{\perp n}^{\text{eff}}$ was assumed in EDGE2D).

separatrix, and to dependence of σ_{Te} on $n(r)$ and $T_e(r)$, apparent from (29b), i.e. $\sigma_{Te} \sim \tau_{\|Te} \propto \chi_{\|e} \propto T_e^{5/2}/n$. In other words, as the plasma cools, parallel electron conduction becomes less efficient at removing the electron heat, leading to a broadening of the near-SOL $T_e(r)$ profile. In comparison, the reduction in advective losses is far less pronounced, $\sigma_n \sim \tau_{\|n} \propto c_s \propto T_e^{1/2}$, such that the broadening of the near-SOL $n(r)$ profile is smaller by roughly a factor of two. This largely explains the ratio $\lambda_n^{\text{near-SOL}}/\lambda_{Te}^{\text{near-SOL}} \approx 2$ observed during high power (low collisionality) discharges on many machines, including JET.

The top frames in figure 4 show the radial profiles of turbulent and collisional radial fluxes of particles and electron energy, normalised by $n_0 c_{s0}$ and $p_0 c_{s0} = n T_{e0} c_{s0}$, respectively. The turbulent fluxes of particles, Γ_r^{turb}, heat, q_r^{turb}, and energy, Q_r^{turb}, are defined as

$$\Gamma_r^{\text{turb}} \equiv \langle n v_x \rangle, \qquad\qquad q_r^{\text{turb}} \equiv \frac{5}{2} \langle n \rangle \langle T_e v_x \rangle, \qquad\qquad (35a)$$

$$Q_r^{\text{turb}} \equiv \frac{5}{2} \langle n T_e v_x \rangle \approx \frac{5}{2} \langle T_e \rangle \Gamma_r^{\text{turb}} + q_r^{\text{turb}}, \qquad\qquad (35b)$$

where $\langle \cdot \rangle$ corresponds to a poloidal-temporal average and Q_r^{turb} is broken down into the convective and conductive contributions; the corresponding collisional (Pfirsch-Schlüter)

fluxes are defined as

$$\Gamma_r^{\mathrm{coll}} \equiv D_{\perp n}^{PS}\langle\nabla_x n\rangle, \qquad q_r^{\mathrm{coll}} \equiv D_{\perp Te}^{PS}\langle n\nabla_x T_e\rangle \approx D_{\perp Te}^{PS}\langle n\rangle\langle\nabla_x T_e\rangle, \qquad (36a)$$

$$Q_r^{\mathrm{coll}} \equiv \frac{5}{2}\langle T_e\rangle\Gamma_r^{\mathrm{coll}} + q_r^{\mathrm{coll}}. \qquad (36b)$$

Note that in (35b) and (36a) we neglect the poloidal-temporal averages of the cross terms $\langle\tilde{n}\tilde{T}_e v_x\rangle$ and $\langle\tilde{n}\nabla_x\tilde{T}_e\rangle$, where $\tilde{\mathscr{A}} = \mathscr{A} - \langle\mathscr{A}\rangle$ denotes the fluctuating part of quantity $\mathscr{A}$.

Since the turbulent fluxes, (35a)-(35b), are two orders of magnitude larger than the collisional fluxes, (36a)-(36b), as is evident from figure 4, we may conclude that radial transport of both particles and energy is entirely dominated by turbulent motions of plasma filaments. Examination of the convective and conductive contributions to the turbulent energy flux (the latter is shown separately in figure 4) reveals the two to be comparable in both the edge and SOL regions. As a consequence of the excessively high $\lambda_n^{\mathrm{far-SOL}}$, the above ESEL simulations significantly overestimate the level of main chamber recycling and energy deposition on outboard limiters in JET, i.e. they predict that roughly half the particles, and one tenth of the energy, crossing the separatrix arrive at the outboard limiters, $\Gamma_r^{\mathrm{turb}}(r_{lim})/\Gamma_r^{\mathrm{turb}}(r_{sep}) \approx 0.58$ and $Q_r^{\mathrm{turb}}(r_{lim})/Q_r^{\mathrm{turb}}(r_{sep}) \approx 0.13$. Although the plasma fluxes to the limiter at the outer mid-plane on JET are difficult to establish accurately, the above values are certainly in excess of those inferred from measured $n(r)$ profiles, assuming a constant effective velocity, see (37b) below, which suggests $\Gamma_r^{\mathrm{turb}}(r_{lim})/\Gamma_r^{\mathrm{turb}}(r_{sep}) \approx 0.06$ at the probe location. Similarly, $j_{sat}(r)$ profiles measured with fast reciprocating probe near the top of the torus, see figures 2 and 5 in [50], which yield $j_{sat}^{\mathrm{turb}}(r_{lim})/j_{sat}^{\mathrm{turb}}(r_{sep}) \approx 0.02$; similar values were inferred previously in [57]. Possible causes of this discrepancy are discussed at the end of the section.

The lower frames in figure 4 show the radial profiles of the *effective diffusivities* of particles and heat, and *effective radial flow velocities* of particles and heat, defined as

$$D_{\perp n}^{\mathrm{eff}} = \frac{\Gamma_r^{\mathrm{turb}}}{\langle\nabla_x n\rangle}, \qquad \chi_{\perp}^{\mathrm{eff}} = D_{\perp T}^{\mathrm{eff}} = \frac{q_r^{\mathrm{turb}}}{\langle n\rangle\langle\nabla_x T_e\rangle} \qquad (37a)$$

$$v_{\perp n}^{\mathrm{eff}} = \frac{\Gamma_r^{\mathrm{turb}}}{\langle n\rangle}, \qquad v_{\perp T}^{\mathrm{eff}} = \frac{2}{5}\frac{q_r^{\mathrm{turb}}}{\langle n\rangle\langle T_e\rangle}, \qquad (37b)$$

With these definitions the turbulent energy flux (35b) can be written in two alternatives forms,

$$Q_r^{\mathrm{turb}} = \frac{5}{2}\langle T_e\rangle D_{\perp n}^{\mathrm{eff}}\langle\nabla_x n\rangle + D_{\perp T}^{\mathrm{eff}}\langle n\rangle\langle\nabla_x T_e\rangle = \frac{5}{2}\langle T_e\rangle\langle n\rangle\left(v_{\perp n}^{\mathrm{eff}} + v_{\perp T}^{\mathrm{eff}}\right) \qquad (38)$$

The effective particle diffusivity (lower left frame in figure 4) is found to increase from ≈ 3 m^2/s on the separatrix to a plateau value of ≈ 10 m^2/s starting at $r - r_{sep} \approx 10$ mm, which persists into the far-SOL and even into the limiter shadow region. The effective heat diffusivity follows a similar profile, but is a factor of 5/2 larger, such that $D_{\perp T}^{\mathrm{eff}} \approx \frac{5}{2}D_{\perp n}^{\mathrm{eff}}$. The effective velocities (lower right frame in figure 4) are found to be roughly constant across the SOL, with $v_{\perp n}^{\mathrm{eff}} \approx 130 - 180$ m/s and $v_{\perp T}^{\mathrm{eff}} \approx 200 - 230$ m/s. It is instructive to compare these results with effective velocities derived based on simple SOL assumptions and average e-folding lengths,

$$\lambda_n \approx v_{\perp n}^{\mathrm{eff}}\tau_{\|n} \approx v_{\perp n}^{\mathrm{eff}}L_{\|}/c_s, \qquad \lambda_T \approx v_{\perp T}^{\mathrm{eff}}\tau_{\|T} \approx v_{\perp T}^{\mathrm{eff}}L_{\|}^2/\chi_{\|e} \qquad (39)$$

Inserting the values of the effective flow velocities, e-folding lengths and parallel loss times, we find these simple SOL expressions to be well satisfied throughout most of the SOL, e.g. $v_{\perp n}^{eff} \tau_{\parallel n} \approx 150$ m/s $\times 25$ m $/77$ km/s ≈ 50 mm $\approx \lambda_n^{SOL}$.

There are two methods in which the above ESEL predictions can be compared to experiment. The first method is to compare directly with the turbulent $\mathbf{E} \times \mathbf{B}$ radial flux profiles in JET Ohmic discharges, inferred from fast reciprocating probe measurements of particle density and potential fluctuations across the SOL [57]; such measurements indicate particle diffusivities of $0.5 - 2$ m^2/s and effective flow velocities of $\approx 50 - 200$ m/s. The second method consists in comparing with edge plasma fluid modeling (e.g. using the EDGE2D code package), in which the radial profiles of $D_{\perp a}^{eff}$ are chosen as to offer the best match to the experimentally measured $n(r)$ and $T_e(r)$ profiles; such modeling indicates particle diffusivities of $0.5 - 1.5$ m^2/s. Unfortunately, neither the first nor the second method offers a measure of radial transport at the outer mid-plane ($\theta = 0$, with θ being the poloidal angle), where it is known to be largest due to *unfavourable* magnetic curvature and where the ESEL computational box is located; it is worth noting that if this box were moved to the inner mid-plane ($\theta = \pi$), where the magnetic field curvature is *favourable* and the edge plasma is stable against interchange instabilities, a similar computation would yield $D_{\perp n}^{eff} = D_{\perp n}^{PS'}$, i.e. a value smaller by roughly two orders of magnitude. Instead, the reciprocating probe measures $D_{\perp n}^{eff}$ and $v_{\perp n}^{eff}$ near the top of the torus ($\theta \approx \pi/2$), while EDGE2D modeling estimates poloidally averaged ($\theta \approx 0 - 2\pi$) values of these quantities. Assuming that radial transport exhibits strong ballooning character, i.e. that $D_{\perp a}^{eff}(\theta = 0) \gg D_{\perp a}^{eff}(\theta = \pi)$, as predicted theoretically and observed in many experiments, that $D_{\perp a}^{eff}(\theta)$ has a maximum at $\theta = 0$ and a poloidal full width at half maximum, $\Delta\theta$, smaller than π (this value was recently inferred as $\Delta\theta/2\pi \approx 1/6$ based on dedicated studies on the Tore Supra tokamak [58]), the poloidally-averaged and outer mid-plane diffusivities may be related as $D_{\perp}^{ave} \approx (\Delta\theta/2\pi)D_{\perp}^{omp} \approx D_{\perp}^{omp}/6$. As a result, the outer mid-plane diffusivity profile may be estimated as $D_{\perp}^{omp}(r) \approx 3 - 9$ m^2/s by multiplying the EDGE2D results by a factor of six. The resulting values, plotted in figure 4, are in fair agreement with ESEL predictions, aside from the far-SOL region, where ESEL overestimates the turbulent radial diffusivitities and/or fluxes by a factor of three.

To conclude the section, let us consider some possible causes of the discrepancy between the predicted and measured SOL particle density profiles. These may be linked to several crude approximations invoked in the ESEL simulations, namely two dimensional geometry (inadequate treatment of parallel transport), finite poloidal box size, cold ion approximation, constant (non-varying) collisional dissipative terms, the neglect of electromagnetic fluctuations and the absence of neutrals and impurities. The first of these items is particularly notable for two reasons:

- the estimate $L_{\parallel n} \approx L_{\parallel T_e} \approx L_{\parallel}$ and $M_{\parallel} \approx 0.5$ invoked in (29a)-(29b) may substantially underestimate the degree of parallel losses. Additional simulations indicate that increasing the Mach number (or decreasing $L_{\parallel n}$) by a factor of two does not substantially alter the density e-folding length (reduced by $\approx 10\%$), presumably because of the related increase of viscous damping and radial transport, implied by $\tau_{\parallel n} = \tau_{\parallel \Omega}$, leads to weaker damping of poloidal flows and hence larger turbulent outflux. Relaxing this assumption,
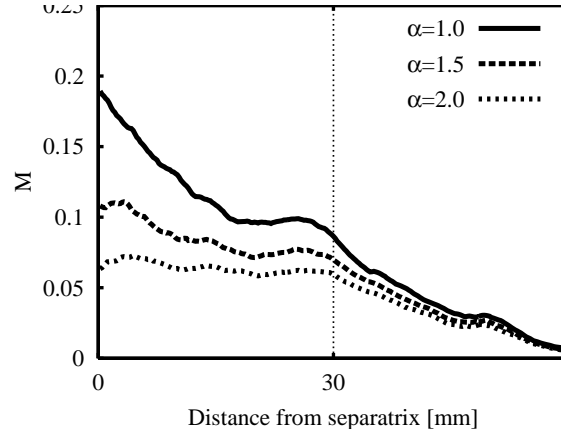
Figure 5. Radial profiles (averaged in time and poloidal direction) of the parallel Mach number at the probe location on TCV calculated using (40) based on the ESEL simulation for TCV relevant parameters. The flow originates at the outer mid-plane and is directed towards both divertor targets. The SOL region corresponds to 0-30 mm outboard of the separatrix, and the wall shadow to 30-60 mm.

one finds roughly $\lambda_n \propto \tau_{\|n} \propto L_{\|n}$, in line with (39), such that the observed discrepancy can be largely removed by assuming $L_{\|n}/L_{\|} \approx r/R_0$. Ideally, parallel transport should be treated by including several grid points along the field line, leading to a fully three dimensional solution,

- the absence of sheath dissipative effects in the ESEL governing equations, which have been replaced by advective momentum loss, as discussed in section 2.2. Since the inclusion of sheath dissipation in interchange dynamics of plasma filaments has been recently shown to decelerate their radial motions [24], inclusion of these effects in the ESEL model, alongside the advective momentum losses, could significantly decrease the far-SOL particle density, and thus improve the agreement with experiment. The inclusion of sheath dissipation is motivated by (i) the advective disspation criterion (9), which while clearly satisfied for TCV, $\tau_\perp/\tau_\| \approx 0.03$, is only moderately satisfied for JET, $\tau_\perp/\tau_\| \approx 0.2$, and (ii) the lower collisionality of JET plasmas compared to TCV, which is reduced by roughly a factor of three, $\nu_e^* \approx 10$ vs. 30.

6.3. Comparison with $\mathbf{B} \times \nabla B$-independent (ballooning) part of the parallel SOL flow in Ohmic and L-mode plasmas

Having demonstrated that ESEL simulations offer a reasonable match to radial profiles of upstream plasma quantities, we next turn to consider the implication of these results to one of the outstanding problems of tokamak edge plasma physics, namely the origin of the $\mathbf{B} \times \nabla B$-independent part of the parallel SOL flow. Such flows were first observed on the DITE tokamak [48], and were since measured on several machines, e.g. at the top of the JET poloidal cross-section ($M_{\|} \approx 0.2$) [50] and at the inner mid-plane of Alcator C-Mod ($M_{\|} \approx 0.5$) [52]. Neither the $\mathbf{B} \times \nabla B$-dependent or independent parts of the parallel SOL flow is presently understood, although the former is thought to be related to Pfirsch-Schlüter
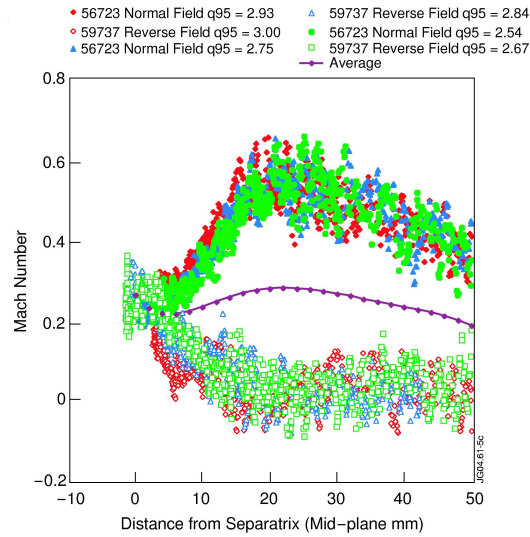
Figure 6. Parallel Mach number measured by a reciprocating Mach probe located near the top of the JET vessel, in normal ($\mathbf{B} \times \nabla B$ towards the X-point) and reverse ($\mathbf{B} \times \nabla B$ away from the X-point) field directions in JET Ohmic plasmas. The average value represents the $\mathbf{B} \times \nabla B$-independent part of the flow, which shows a clear ballooning character (positive values indicate flow towards the inner divertor). Reproduced from [50] (figure 6).
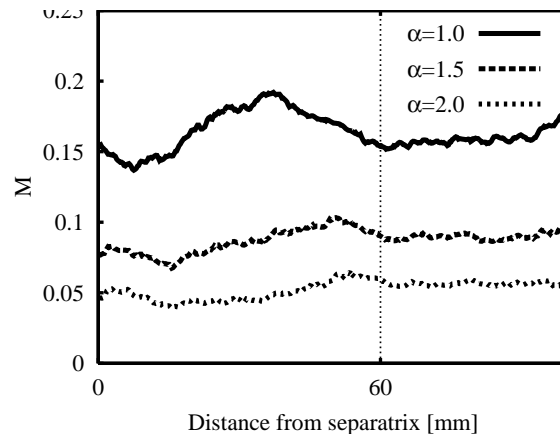

Figure 7. Similar to figure 5 only for JET relevant conditions. The results should be compared with figure 6. The flow originates at the outer mid-plane and is directed towards both divertor targets. The SOL region corresponds to 0-60 mm outboard of the separatrix, and the limiter shadow to 60-100 mm.

parallel return flow, see figure 1. A clear understanding of the $\mathbf{B} \times \nabla B$-independent part has yet to emerge [50, 52, 53]. In fact, very little is known about this mechanism aside from its strong *ballooning* character which is thought necessary to create the SOL recirculation from the outer mid-plane to both divertor targets.

Interchange turbulence, being driven by unfavourable magnetic curvature, offers a natural explanation for the observed ballooning character of the outward fluxes. Since magnetic curvature, $\mathbf{b} \cdot \nabla \mathbf{b}$, is independent of the $\mathbf{B} \times \nabla B$ direction, it would account for both

the direction of the observed *sub-sonic* flow (from the outer mid-plane towards both divertor targets) and the lack of dependence on the toroidal field direction; effectively, as a plasma blob drifts across any given flux tube, it perturbs the local pressure and launches a sound wave towards both divertor targets, in line with equations (28). In this physical picture, the time-averaged magnitude of the $\mathbf{B} \times \nabla B$-independent flow (which is the experimentally available quantity) represents the time-average of (i) the sub-sonic flow (with $M_\parallel \approx 0.5$) during the intermittent outward bursts of large plasma blobs, in which the local pressure exceeds the flux-tube average value by some factor α and acoustic pulses are launched in response to the local parallel pressure gradient $\nabla_\parallel p$, and (ii) the largely stagnant SOL flow (with $M_\parallel \ll 0.5$) during the quiescent phase, in which the pressure is below the flux tube average value and roughly along the flux tube in the upstream SOL. The two flow conditions correspond to the simple SOL, in which sub-sonic flow is driven by upstream source of particles, and the recycling SOL, in which the source of particles is restricted to target recycling (recall that the upstream SOL flow velocity tends to vanish in the absence of radial sources and Pfirsch-Schlüter flows).

The above arguments rely on a global balance of particles and parallel momentum in any given flux tube, (27), and therefore require appropriate sink terms for each acoustic pulse launched by an outward drifting plasma filament. Such a pulse may terminate at the divertor targets, which act as an effective sink for all plasma flows, or may drift inward/outward onto a different flux tube (perhaps crossing the separatrix to return to the region of closed field lines) which acts as a volumetric sink within that flux tube. The importance of such volumetric sinks for the ballooning-like SOL flow was demonstrated by recourse to global plasma fluid modeling of the edge plasma [56], using the EDGE2D/NIMBUS code. In the context of turbulence (ESEL) simulations considered here, which are both two dimensional and local, the specification of particle density and temperature at the inner boundary of the computational box, implicitly assumes sufficient influx of plasma and neutrals (across the separatrix surface) to balance the ballooning-like out flux as predicted by the ESEL code. In short, the simulations do not address the global distribution of source and sinks and the associated flow patterns.

To estimate the effect of turbulence driven flows from ESEL simulations, we must therefore resort to a simplifying *Ansatz*, whose validity should later be tested by comparison with a three dimensional calculation. We thus estimate the time-averaged Mach number as the product of the sub-sonic value of 0.5 and the fraction of the time that a significant parallel pressure gradient exists in the flux tube. In the absence of parallel profiles, we approximate the latter by a time-averaged pressure, which we denote by $\langle p \rangle$, and write

$$\langle M_\parallel \rangle \approx 0.5 f_{p>\alpha\langle p \rangle}, \qquad f_{p>\alpha\langle p \rangle} \equiv \frac{t(p > \alpha\langle p \rangle)}{\Delta t} \tag{40}$$

Here 0.5 represents the sub-sonic $M_\parallel$, Δt is the total time of the simulation, $t(p > \alpha\langle p \rangle)$ is the total time during which the local pressure exceeds α times the time-averaged local pressure, and $f_{p>\alpha\langle p \rangle}$ is the fraction of the time that this conditions is satisfied. Based on (28), which neglects viscous effects and momentum sources/sinks, we expect α to be a constant approximately equal to unity, $\alpha \approx 1$.

The criterion of equation (40) has been applied to the ESEL simulations of TCV Ohmic and L-mode plasmas discussed in section 6.1 (where the damping coefficients recommended

by the analysis of this paper have been used) [11]. The radial profiles of $M_\parallel$, are calculated on the basis of equation (40) applied to local n and T_e, after which they are averaged poloidally and in time. The results are plotted in figure 5 for three values of α. One finds $M_\parallel \approx 0.2 - 0.05$ across the SOL for $\alpha = 1 - 2$. This range of values has been found in parallel SOL flow measurements on TCV [54], where a $\mathbf{B} \times \nabla B$-independent component of $M_\parallel \approx 0.1$ in the ballooning direction (away from the outer mid-plane) has been recently found in toroidal field reversal experiments.

Similar comparison can also be performed for JET Ohmic and L-mode discharges discussed in section 6.2, for which radial profiles of the parallel Mach number have been measured with a reciprocating Mach probe (see figure 6 in [50], which is reproduced here as figure 6). The $\mathbf{B} \times \nabla B$-independent contribution is estimated by taking the average of the forward and reversed field directions, with the result $M_\parallel \approx 0.2 - 0.3$. The parallel Mach number $M_\parallel$ profile corresponding to figure 3 is calculated using (40) for three values of α and is plotted in figure 7. The Mach number is predicted as $M_\parallel \approx 0.2$ for $\alpha \approx 1$, in good agreement with the measured value, figure 6.

7. Conclusions

First principles expressions for the damping terms in collisional scrape-off layer turbulence have been derived based on neoclassical perpendicular transport (Pfirsch-Schlüter diffusion) and classical parallel transport (sub-sonic advection and Spitzer-Härm diffusion) of mass, momentum and energy. The final set of coefficients, expressed in Bohm normalised form, is given by equations (20) and (27).

Two notable differences with commonly used damping terms have been identified: (i) momentum diffusivity, and the associated viscous dissipation, have been shown to be much larger than the particle diffusivity, and (ii) it has been argued that the assumption of sheath-dissipative damping of vorticity is inappropriate under collisional conditions, and that it should be replaced by a sub-sonic, advective loss. The predicted expressions derived here for the damping terms successfully predict the level of dissipation required to reproduce the SOL turbulence statistics, temporal correlations and radial profiles measured on the TCV tokamak [11]. They also reproduce, with reasonable accuracy, the radial SOL profiles of particle density and temperature in JET Ohmic and L-mode discharges, although the far-SOL particle density e-folding length is over-estimated by a factor of three. On the basis of this agreement, we may conclude that turbulent SOL transport (at least in TCV and JET Ohmic and L-mode plasmas) is driven by interchange motions (related to unfavourable magnetic curvature and radial pressure gradients in the edge region) and is influenced by neoclassical collisional diffusion and parallel conductive and convective losses in the SOL region. The interchange model discussed here provides a first principles understanding of SOL mass, momentum and energy transport and contains only few adjustable parameters, e.g. $M_\parallel, L_{\parallel n}, L_{\parallel \Omega}, L_{\parallel T_e}$ and the size of the computational domain. Most importantly, it suggests that SOL turbulence is dominated by electrostatic (drift-ordered) plasma dynamics, since good agreement with experimental data (in fact an overestimate of radial transport!) is obtained

without including the effect of fluctuating magnetic fields.

The above physical picture offers new insight into two important classes of observations in tokamak experiments. First, it effectively reconciles any apparent inconsistencies between the presence of upstream SOL fluctuations and the (neo)classical scaling of radial profiles of deposited power on JET divertor targets [40] – this scaling simply reflects the neoclassical dissipation of SOL turbulence. Although this conclusion was anticipated in [22] based on analysis of the dissipative scale of SOL turbulence, the ESEL study increases the credibility of this type of analysis. Second, transient, sub-sonic *parallel* advection in response to curvature-driven *radial* excursions of turbulent plasma blobs (or filaments) appears to offer a viable mechanism for the $\mathbf{B} \times \nabla B$-independent (ballooning) part of the parallel SOL flow that has now been measured in a number of tokamaks [50, 52, 54]. This flow is interpreted as the temporal average of the largely stagnant ($M \approx 0$) recycling dominated SOLduring the quiescent phase between the bursts, and the sub-sonic ($M_\parallel \approx 0.5$) transient pulse propagation driven by parallel pressure gradients due to intermittent outward bursts of turbulent filaments (or blobs). Comparison with TCV and JET measured parallel Mach numbers appears to support the above hypothesis.

Acknowledgments

References

[1] Zweben S J and Gould R W 1985 *Nucl. Fusion* **25** 171

[2] Wootton A J, Carreras B A, Matsumoto H, McGuire K, Peebles W A, Ritz Ch P, Terry P W and Zweben S J 1990 *Phys. Fluids B* **2** 2879

[3] Endler M 1999 *J. Nucl. Mater.* **266–269** 84

[4] Sánchez E, Hidalgo C, López-Bruna D, García-Cortés I, Balbín R, Pedrosa M A, Riccardi C, Chiodini G, Bleuel J, Endler M, Carreras B A and Newman D E 2000 *Phys. Plasmas* **7** 1408

[5] Boedo J A, Rudakov D, Moyer R, Krasheninnikov S, Whyte D, McKee G, Tynan G, Schaffer M, Stangeby P, West P, Allen S, Evans T, Fonck R, Hollann E, Leonard A, Mahdavi A, Porter G, Tillack M and Antar G 2001 *Phys. Plasmas* **8** 4826

[6] Antar G, Counsell G, Yu Y, Labombard B and Devynck P 2003 *Phys. Plasmas* **10** 419

[7] Zweben S J, Maqueda R J, Stotler D P, Keesee A, Boedo J, Bush C E, Kaye S M, LeBlanc B, Lowrance J L, Mastrocola V J, Maingi R, Nishino N, Renda G, Swain D W, Wilgen J B and the NSTX Team 2004 *Nucl. Fusion* **44** 134

[8] Graves J P, Horacek J, Pitts R A and Hopcraft K I 2005 *Plasma Phys. Control. Fusion* **47** L1

[9] Horacek J, Pitts R A and Graves J P (2005) *Czechoslovak Journal of Physics* **55** 271

[10] Horacek J, Garcia O E, Graves J P, Pitts R A, Nielsen A H, Naulin V and Rasmussen J J 2005 *Europhys. Conf. Proc.* **29C** O-4.004, 32nd EPS Conference on Plasma Physics, Tarragona, Spain

[11] Garcia O E, Horacek J, Pitts R A, Nielsen A H, Fundamenski W, Graves J, Naulin V and Rasmussen J J 2006 *Plasma Phys. Control. Fusion* , **48** L1

[12] Garcia O E, Naulin V, Nielsen A H and Rasmussen J J 2004 *Phys. Rev. Lett.* **92** 165003

[13] Garcia O E, Naulin V, Nielsen A H and Rasmussen J J 2005 *Phys. Plasmas* **12** 062309

[14] Garcia O E, Naulin V, Nielsen A H and Rasmussen J J 2006 *Physica Scripta* **T122** 89

[15] Motley R W 1981 *Nucl. Fusion* **21** 1541

[16] Nedospasov A V 1989 *Sov. J. Plasma Phys.* **15** 659

[17] Sarazin Y and Ghendrih Ph 1998 *Phys. Plasmas* **5** 4214

[18] Sarazin Y, Ghendrih Ph, Attuel G, Clément C, Garbet X, Grandgirard V, Ottaviani M, Benkadda S, Beyer P, Bian N and Figarella C 2003 *J. Nucl. Mater.* **313–316** 796

[19] Ghendrih Ph, Sarazin Y, Attuel G, Benkadda S, Beyer P, Falchetto G, Figarella C, Garbet X, Grandgirard V and Ottaviani M, 2003 *Nucl. Fusion* **43** 1013

[20] Ribeiro T T and Scott B 2005 *Plasma Phys. Control. Fusion* **47** 1657

[21] Stangeby P C 2000 *The Plasma Boundary of Magnetic Fusion Devices* (Plasma Physics Series) (Institue of Physics Publishing, Bristol, UK)

[22] Fundamenski W, Pitts R A, Matthews G F, Riccardo V, Sipilä S and JET EFDA Contributors 2005 *Nucl. Fusion* **45** 950

[23] Garcia O E, Bian N H, Naulin V, Nielsen A H and Rasmussen J J 2005 *Phys. Plasmas* **12** 090701

[24] Garcia O E, Bian N H and Fundamenski W 2006 submitted to *Phys. Plasmas*

[25] Kukushkin A et al 2003 *Nucl. Fusion* **43** 942

[26] Braginskii S I 1965 *Rev. Plasma Phys.* **1** 205

[27] Huba J D 2002 *NRL Plasma Formulary* (Naval Research Laboratory, Washington, DC)

[28] Miyamoto K 1987 *Plasma Physics for Nuclear Fusion* (Cambridge, Massachusetts: MIT Press)

[29] Hazeltine R D and Meiss J D 1992 *Plasma Confinement* (Addison–Wesley, New York)

[30] Hazeltine R D and Waelbroeck F L 2004 *The Framework of Plasma Physics* (Westview Press, Boulder, CO)

[31] Helander P and Sigmar D J, 2002 *Collisional Transport in Magnetized Plasmas*, (Cambridge U Press, Cambridge)

[32] Wesson J, 1997 *Tokamaks*, (Oxford U Press, Oxford, UK)

[33] Ichimaru S, 1992 *Statistical Plasma Physics*, (Addison–Wesley, New York)

[34] Spitzer L, 1956 *The Physics of fully ionized gases*, (Interscience, New York)

[35] Goldston R J and Rutherford P H, 1995 *Introduction to Plasma Physics*, (IoP Press, Bristol, UK)

[36] Garcia O E, Bian N H, Paulsen J-V, Benkadda S and Rypdal K 2003 *Plasma Phys. Control. Fusion* **45** 919

[37] Garcia O E and Bian N H 2003 *Phys. Rev. E* **68** 047301

[38] Bian N H and Garcia O E 2003 *Phys. Plasmas* **10** 4696

[39] Pfirsch D and Schlüter A 1962 *Max-Planck Institute Report* MPI/PA/7/62

[40] Fundamenski W, Sipilä S and JET-EFDA Contributors 2004 *Nucl. Fusion* **44** 20

[41] Spitzer L and Härm R 1953 *Phys. Rev.* **89** 977

[42] Fundamenski W 2005 *Plasma Phys. Control. Fusion* **47** R163

[43] Fundamenski W, Pitts R A and JET EFDA Contributors *Plasma Phys. Control. Fusion* 2006 *Plasma Phys. Control. Fusion* **48** 109

[44] Pitts R A, Fundamenski W and JET EFDA Contributors 2006 *Nucl. Fusion* **46** 82

[45] Thomsen H, Endler M, Bleuel J, Chankin A V, Erents S K and Matthews G F (2002) *Phys. Plasmas* **9** 1233

[46] Gombosi T I 1994 *Gaskinetic Theory* (Cambridge: Cambridge University Press)

[47] Whyte D G, Lipschultz B L, Stangeby P C, Boedo J, Rudokov D L, Watkins J G and West W P 2005 *Plasma Phys. Control. Fusion* **47** 1579

[48] Pitts R A *et al* 1990 *J. Nucl. Mater.* **176-177** 893

[49] Lipschultz B, Whyte D and LaBombard B 2005 *Plasma Phys. Control. Fusion* **47** 1559

[50] Erents K, Pitts R A, Fundamenski W, Gunn J P and Matthews G F 2004 *Plasma Phys. Control. Fusion* **46**

1757

[51] Erents K, Stangeby P C 1998 *Nucl. Fusion* **38** 1637

[52] LaBombard B, Rice R J, Hubbard A E, Hughes J W, Greenwald M, Irby J, Lin Y, Lipschultz B, Marmar E S, Pitcher C S, Smick N, Wolfe S M, Wunkitch S J and the Alcator Group 2004 *Nucl. Fusion* **44** 1047

[53] Asakura N, Takenaga H, Sakurai S, Porter G D, Rognlien T D, Rensink M E, Shimizu K, Higashijima S and Kubo H 2004 *Nucl. Fusion* **44** 503

[54] Pitts R A, Horacek J *et al* 2006 in preparation for *J. Nucl. Mater.*

[55] Erents S K, Stangeby P C, LaBombard B, Elder J D and Fundamenski W (2000) *Nucl. Fusion* **40** 295

[56] Kirnev G, Corrigan G, Coster D, Erents S K, Fundamenski W, Matthews G F and Pitts R A 2005 *J. Nuclear Mater.*, **337-339**, 2005, 271

[57] Garcia-Cortes I, Loarte A, Balbin R *et al* 2001 *J. Nucl. Mater.* **290–293** 604

[58] Gunn J *et al* 2006 in preparation for *J. Nucl. Mater.*